Computationally efficient model to predict the deformations of a cellular foot orthotic

Mohammadreza Moeini[a], **Anne-Laure Ménard**[b,c], **Lingyu Yue**[a], **Maryam Hajizadeh**[b], **Mickael Begon**[b,c], **Martin Lévesque**[a,*]

[a] *Laboratory for Multiscale Mechanics, Polytechnique de Montréal, Montréal, Québec H3C3A7, Canada*

[b] *Laboratory of Simulation and Movement Modelling, School of Kinesiology and Physical Activity Sciences, Québec, Canada.*

[c] *CHU Sainte-Justine - Research Center, Québec, Canada.*

Abstract

Background: Foot orthotics (FOs) are frequently prescribed to provide comfortable walking for patients. Finite element (FE) simulation and 3D printing pave the way to analyse, optimize and fabricate functionally graded lattice FOs where the local stiffness can vary to meet the therapeutic needs of each individual patient. Explicit FE modelling of lattice FOs with converged 3D solid elements is computationally prohibitive. This paper presents a more computationally efficient FE model of cellular FOs. **Method:** The presented FE model features shell elements whose mechanical properties were computed from the numerical homogenization technique. To verify the results, the predictions of the homogenized models were compared to the explicit model's predictions when the FO was under a static pressure distribution of a foot. To validate the results, the predictions were also compared with experimental measurements when the FO was under a vertical displacement at the medial longitudinal arch. **Results:** The verification procedure showed that the homogenized model was 46 times faster than the explicit model, while their relative difference was less than 8% to predict the local minimum of out-of-plane displacement. The validation procedure showed that both models predicted the same contact force with a relative difference of less than 1%. The predicted force-displacement curves were also within a 90% confidence interval of the experimental measurements having a relative difference smaller than 10%. In this case, using the homogenized model reduced the computational time from 22 hours to 22 minutes. **Conclusion:** The presented homogenized model can be therefore employed to speed up the FE simulation to predict the deformations of the cellular FOs.

Keywords: Foot orthotics, Finite Element Method, Homogenization, 3D printing, Digital Image Correlation

[*] **Corresponding author:** M. Lévesque (martin.levesque@polymtl.ca)

Highlights

- We introduced a computationally efficient FE model of a honeycomb lattice foot orthotic by numerical homogenization.
- The homogenized model's prediction is verified by the explicit model's prediction and validated by the experimental measurements.
- The homogenized model predicts the same displacement field as the explicit model, but it is 46 times faster.
- In a contact simulation, the homogenized model predicts the force-displacement curve 60 times faster than the explicit model. The relative difference between their predictions is less than 1.0%.
- Both models predict a contact force close to the experimental results with a relative difference smaller than 10%.

1 Introduction

Orthopedic insoles or foot orthotics (FOs) are one of the most common devices prescribed to mitigate the difficulties associated with foot disorders [1] or to alleviate the risk of feet ulcers, which is a source of major suffering for diabetic patients [2]. This motivates researchers to design customized FOs to obtain functional orthoses that satisfy the biomechanical needs of each specific patient. Besides, Three-Dimensional (3D) printing paves the way to manufacture patient-specific and affordable FOs featuring customizable mechanical properties and complex geometries [3, 4]. Customized mechanical properties can be obtained by cellular structures. In 3D printed cellular FOs, the cell dimensions can be locally modified to provide a functionally-graded component whose mechanical response meets the patient-specific therapeutic needs.

Finite Element (FE) simulations could also provide insights into the interaction between foot, FO and shoe. Some researchers focused on FE simulation and geometrical optimization of 3D printed lattice FOs for diabetic patients. The critical factor in designing diabetic FOs is the contact stress between the foot and the FO [5]. Tang et al. [6] optimized the stress distribution of contact surfaces between the foot and the diabetic FO by conducting FE simulations and using 3D printed functionally graded materials. They found that the customized FO reduced the peak contact pressure by approximately 35%. Although their study has had positive contributions in designing and optimizing diabetic FOs, in their validation, there was approximately a relative difference of 50% between the experimentally measured equivalent stiffness and that predicted by the FE model. Moreover, in their optimization, their objectives have been limited to control the static pressure distribution of the foot over the FO. However, prescribed FOs for treating other pathological symptoms do not follow the same objective. In designing FOs for the flat feet condition, for instance, the key is to avoid the excessive collapse of the longitudinal arch to develop an efficient propulsion during gait [1]. To design such insoles, the FE simulation, therefore, should accurately predict the deformation of the cellular insoles under the pressure distribution of the foot.

The FE simulation of cellular insoles should be also efficient in terms of computations. Computational efficiency is important for the optimization application in which iteratively running a large-scale and detailed FE simulation of a lattice structure with a converged 3D mesh is computationally prohibitive, even with modern computers [7, 8, 9]. Moreover, for instance, the optimization's objective might be the outcome of a FE simulation including a patient's foot topology and the cellular FO. In this case, the literature shows that the FE simulation of a foot having nonlinear material properties and complex geometry takes 17 hours using a computer with an Intel® Core™ i7-6700 CPU @ 3.4 GHz and 32 GB RAM [10]. Adding a cellular FO to such a complex biomechanical system would make the simulation even more time-consuming. The computational time is important because simulations in biomechanics often require real-time computing [11]. The urgent nature of clinical problems demands reliable and fast computations [12]. To the best of our knowledge, there is no literature reporting a computationally efficient and experimentally validated FE model of a functionally graded cellular FOs.

The objective of this study was therefore to provide this computationally-efficient FE model (called *surrogate* in the context of optimization) to characterize and predict the mechanical behaviour of a honeycomb lattice FO. We demonstrated that the homogenized FE

model of a honeycomb lattice FO is able to predict the displacement field with almost the same level of accuracy as the explicit FE model featuring 3D elements, for a fraction of the computational cost. Within this context, Section 2 presents the numerical homogenization technique to compute the effective mechanical properties of lattice structures which leads to build and develop our surrogate model. Section 3 presents the verification and validation procedures of the surrogate's predictions. Section 4 discusses the simulation and experimental results and, finally, Section 5 presents the conclusions and contributions of this modelling.

2 Background

2.1 Homogenization technique

Homogenization delivers the effective mechanical properties of a heterogeneous material using the mechanical behaviour of its microstructure. The homogenized model should be able to predict the same mechanical response as that of the heterogeneous structure represented by an explicit fully meshed model when both of them are submitted to the same loading and boundary conditions. Figure 1 schematically shows the application of the homogenized FE model of honeycomb lattice FO under the pressure distribution of the foot.

Numerical homogenization is one of the most common ways to compute the effective properties of a heterogeneous material. In numerical homogenization, the microstructure is explicitly meshed, and then by applying six orthogonal strain tensors, all components of the effective stiffness tensor ($\bar{C}_{ijkl}$) are computed through a volume integration of stress and strain over the entire microstructure. In cellular materials, the microstructure is heterogeneous since it consists of solid and void phases [13]. It is common to assign comparatively soft material properties to the void phase to avoid the numerical difficulties to compute the average strain and stress over the entire microstructure under the applied boundary conditions [14, 15, 16].

Periodic Boundary Conditions (PBC) are the most computationally efficient boundary conditions to provide the effective properties for a heterogeneous material [17, 18]. For heterogeneous materials having a periodic microstructure, such as cellular materials, applying PBC requires only one unit cell to mesh. PBC is then satisfied by

$$\mathbf{u}(\mathbf{x_2}) - \mathbf{u}(\mathbf{x_1}) = \mathbf{E} \cdot (\mathbf{x_2} - \mathbf{x_1}), \tag{1}$$

where $\mathbf{E}$ is the macroscopic strain, and $\mathbf{u}(\mathbf{x_1})$ and $\mathbf{u}(\mathbf{x_2})$ represent the displacement vectors of two corresponding nodes on opposite faces of the unit cell whose location vectors are $\mathbf{x_1}$ and $\mathbf{x_2}$. Corresponding nodes means two nodes sharing the same in-plane coordinates for two surfaces with the same normal. Note that applying Equation (1) requires a periodic mesh over the two opposite sides [19, 20, 21].

2.2 Critical factor in designing insoles for flat feet

For patients with flat feet, clinicians seek to reduce rearfoot eversion and longitudinal arch collapse. A recent study has shown that the deformation of customized FOs at the medial arch region is related to excessive rear-foot eversion, longitudinal arch collapse and abnormal plantar pressure distribution in flat foot individuals [22]. It has been shown that insoles with arch support are more efficient in reducing rear-foot eversion during walking than flat insole [23]. Xu et al. also reported that 3D printed insoles having arch support could provide better comfort for patients with symptomatic flatfoot than prefabricated insoles [24]. Moreover, FOs with customized mechanical features support more efficiently the medial longitudinal arch from collapsing when compared to prefabricated FOs in flat foot participants [25]. Consequently, the critical factor in designing FO for flat feet condition was assumed to be the FO deformation, especially at the medial arch, rather than foot plantar pressure such as in diabetic patients [6].

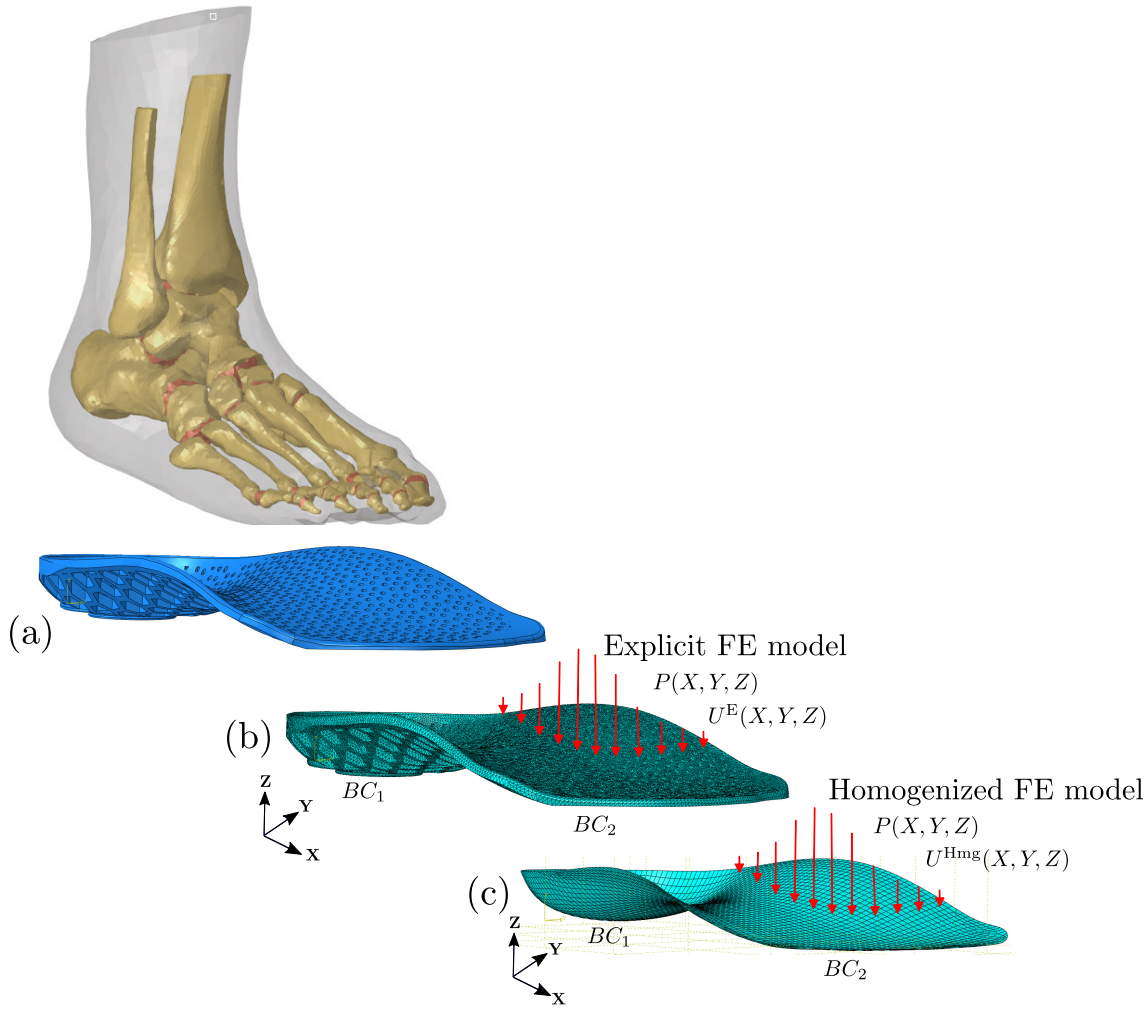

Figure 1: Schematic representation of the application of a homogenized foot orthotics under the pressure distribution of a foot; (a) The CAD file of the designed FO, (b) explicit FE model of the FO that was meshed with 3D solid elements, (c) the homogenized FE model of the FO featuring shell solid elements whose mechanical properties are computed from numerical homogenization. Both FE models are submitted to the same pressure distribution of the foot ($P(X,Y,Z)$) and boundary conditions (BC_1 and BC_2). The predicted displacement field by the homogenized model ($U^{\mathrm{Hmg}}(X,Y,Z)$) should be therefore approximately equal to the predicted displacement field by the explicit model ($U^{\mathrm{E}}(X,Y,Z)$). The explicit model then can be replaced by the homogenized model to speed up the simulation.

3 Methods

3.1 Geometrical description of the foot orthotics

We have designed a honeycomb lattice FO that can provide support to the longitudinal arch of flat feet. Figure 2 schematically shows the geometrical details of this honeycomb lattice FO. The biomechanical and clinical performance of this FO has been already discussed and

published in [4, 26, 22].

The FO consisted of two layers. The first layer, with a height of h_1, was an infilled layer with a distribution of circular holes with a diameter of d. These holes were actually required for ventilation purposes during walking or running. The second layer, with a height of h_2, was a reinforced layer with a honeycomb lattice for the purpose of increasing the insole's rigidity to support the longitudinal arch of the foot. Figure 3 shows the geometrical parameters of a periodic unit cell within the FO structure. The horizontal and inclined hexagon side lengths are h_b and l_b, the wall thickness is t and the angle between vertical and inclined hexagon sides is θ. Furthermore, the hexagon outer side lengths are l and h, which can be explicitly computed by $l = l_b + t/(2\cos\theta)$ and $h = h_b + t(1 - \sin\theta)/\cos\theta$. Using these geometrical parameters, the relative density ρ for a honeycomb unit cell is computed as per [27]:

$$\rho = 1 - \frac{l_b(h_b + l_b \sin\theta)}{l(h + l\sin\theta)}. \tag{2}$$

The relative density ρ directly effected the homogenized mechanical properties of a honeycomb cell. Besides the effective properties, the height of h_1 and h_2 can be also locally varied to change the stiffness of the structure. In this work, a constant height of $h_1 = 1.5$ mm and a variable height of h_2 were considered. In addition, the homogenized mechanical properties are affected by the cell topology. For instance, the literature shows that for the same relative density, square and triangular cells result in stiffer in-plane effective properties when compared to the honeycomb cell [28]. In this research, two other insoles featuring square and triangular cells were also designed and studied, as illustrated in Figure 4. For the square cell having a wall thickness of t and a side length of l_b, ρ is computed by:

$$\rho = \frac{t\,(t + 2l_b)}{(t + l_b)^2}. \tag{3}$$

For the triangular cell having a wall thickness of t and a triangle's side length of l_b, ρ is:

$$\rho = \frac{\Big(3(t/l_b) + \sqrt{3}\Big)\Big(1 + (t/l_b)\sqrt{3}\Big) - l_b\sqrt{3}}{\Big(3(t/l_b) + \sqrt{3}\Big)\Big(1 + (t/l_b)\sqrt{3}\Big)}. \tag{4}$$

3.2 Experiments

3.2.1 Material and manufacturing

The honeycomb lattice FOs were fabricated by Selective Laser Sintering (SLS) from *Shape-Ways* company. The insole's material was Nylon-12 which is one of the most common materials used in SLS 3D printing [29]. The elastic modulus of the Nylon-12 was measured through tensile testing of dog-bone specimens. The dog-bone specimens were type `I` according to `ASTM-D638` standard and manufactured by SLS 3D printing employing the same company. Due to the fact that 3D printing orientation affects the mechanical properties, two types of specimens with different 3D printing orientations including longitudinal (in direction of the tensile test) and transverse directions were considered. Five specimens of each type were manufactured. The printed specimens were tested using an *MTS Insight* electromechanical

tensile machine under displacement-control at a loading rate of 5 mm/min. The reaction force was measured through a load cell of 50 kN. Next, the Young's modulus (E) and the Poisson's ratio (ν) of the specimens were computed.

3.2.2 Foot orthotics under a pressure distribution of foot

The first experiment was testing the honeycomb FO with a relative density of 40% in gait analysis of a 37 years old male participant having normal feet with size of 43 during walking with FOs on a treadmill. The participant's Body Mass Index (BMI) was 27 kg/m^2 (height of 174 cm and weight of 82 kg). The pressure distributions of feet over FOs were measured during 23 walking cycles. Each FO was put in standard sports shoes (*New Balance 860 v8*). The pressure insole *Medilogic WLAN* were placed on the plantar surfaces of the FOs. The sensors recorded plantar pressure distributions with a frequency of 400 Hz. As a result, the measured plantar pressure included 23 walking cycles normalized to 101 time frames. Only the pressure distribution of time frame of 50 was considered in this work, which corresponds to the pressure at the mid-stance phase. The mean pressure distribution was then computed from the 23 cycles.

3.2.3 Foot orthotics under concentrated force

We conducted a compression test over the honeycomb insole with a relative density of $\rho = 40\%$ and using an *MTS Insight* electromechanical machine. Figure 5 shows this experimental setup. It should be noted that this setup does not correspond to the same loading and boundary conditions when the FO is in contact with the shoe and the foot during walking. However, it enabled to accurately measure the displacement and the FO's reaction force, simultaneously. The displacement was imposed over one point at the medial longitudinal arch

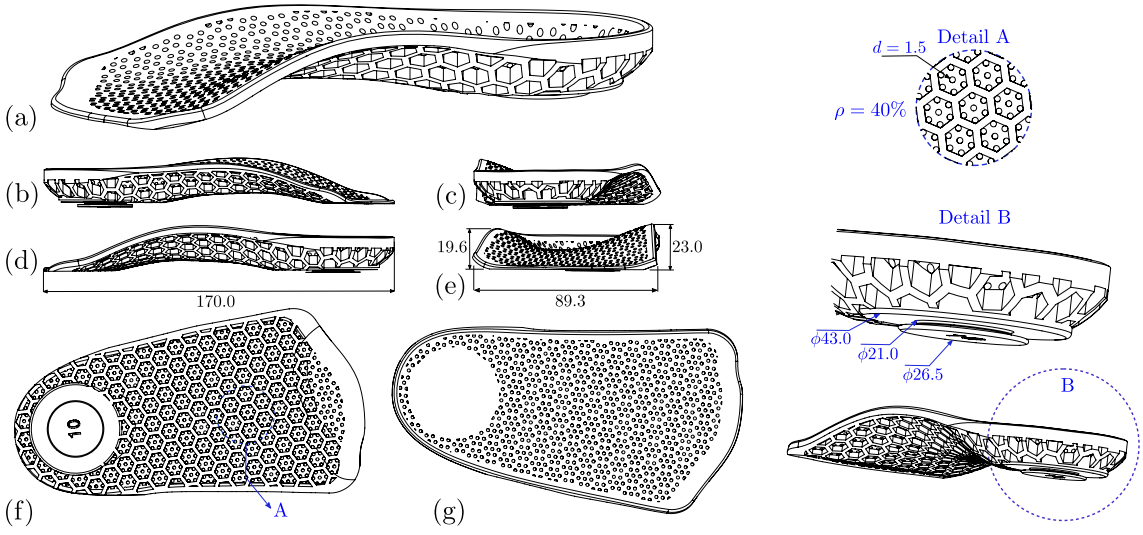

Figure 2: Geometrical details of the designed honeycomb FO; (a) isometric view, (b) left view, (c) back view, (d) right view, (e) front view (f) bottom view, and (g) top view of the FO. The dimensions are in mm and the relative density of the honeycomb cell is 40%.

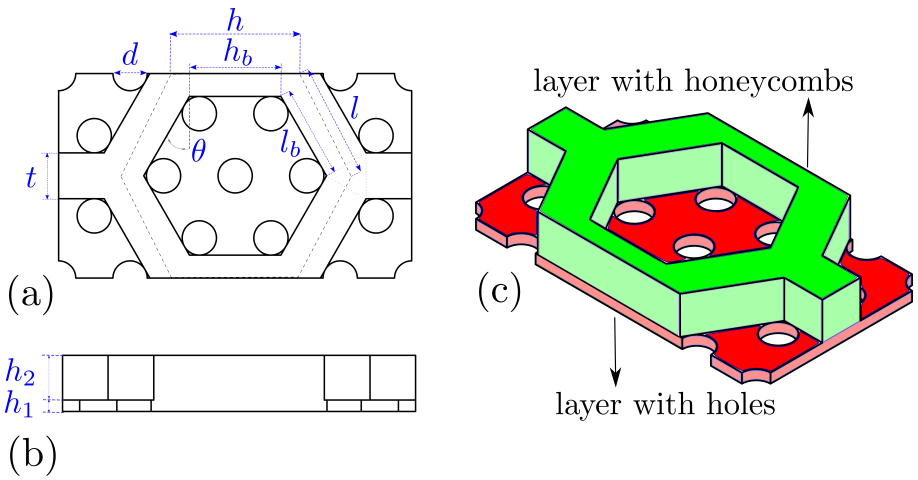

Figure 3: Schematic of the FO's honeycomb unit cell; (a) top view, (b) front view and (c) isometric view. The geometrical parameters (t, l, θ, d, h_1 and h_2) can be locally varied to provide a functionally graded cellular FO. In this study, we considered $\theta = \pi/6$, $l_b = h_b$, $l = h$ and $d = 1.5$ mm. The unit cell is divided into two separated layers; a layer with honeycombs and a layer with holes. The effective properties of each layer were computed by numerical homogenization. The layers were then assembled according to the classical lamination theory to build the surrogate model.

and at the edge of the insole. This point was considered for two reasons. First, it was assumed that the critical factor in designing FOs for flat feet is to avoid the collapse of the longitudinal arch. Thus, the force-displacement curves of a point at the medial longitudinal arch obtained from experimental measurements and predicted by the computational simulation were the system response quantity of interest. Second, the literature shows that, during walking, the maximum out-of-plane displacement of the insole is in the medial longitudinal arch region [26]. Applying loading at this point, therefore, might deliver a global displacement field closer to the actual FO deformation during walking. The loading was applied with the rate of 5 mm/min through a blunt-ended steel punch. The diameter of the punch at the contact point was approximately of 2.0 mm. The FO was fixed at the heel part using a C-clamp, while the fore-foot was free. The test was repeated three times. Each time, the FO and the clamped boundary condition were re-installed to account for the uncertainty of manual installation. The displacement and the reaction force at the contact point were measured with the MTS machine using a load cell of 1 kN. Our validation metric was defined as the contact force between the punch and the insole with respect to the vertical displacement of the punch. Moreover, to evaluate the machine's precision, we also recorded the displacement by the Digital Image Correlation (DIC) technique.

3.2.4 Digital image correlation technique

DIC is a contact-less optical technique to measure the full displacement field by comparing two images of the undeformed and deformed structure under loading [30, 31]. To perform this comparison, the area of interest is painted in white and coated with a black dots pattern.

In our test, the insole's edge was painted with a thin layer of white spray using Painter's Touch® 2X Ultra Cover paint spray. The speckle pattern was then applied over the surface with an airbrush and *Golden Fluid Acrylics Carbon* Black ink. The punch was also covered by white paint and black dots patterns (as shown in Figure 5) to track its displacement.

In the insole, the area of interest was limited to the longitudinal arch since it was difficult to capture its whole displacement field due to the lack of pixels within its thin thickness. The two cameras were placed close to the specimen (about 30 cm) and a 10 mm lens extension was employed. The cameras were then calibrated to determine the extrinsic parameters (e.g., distance between cameras and the specimen) and the intrinsic parameters (e.g., focal length). The displacement fields were extracted during the whole load history using the calibration data and the commercial software *Vic-3D*™ (version 7.2.4). Figure 6 shows three points in the area of interest, as well as the corresponding nodes in the FE models having approximately the same positions. The predicted vertical displacements at these nodes were compared against the experimental measurements for the purpose of validation of the numerical simulations.

3.3 Numerical simulations

Two FE models were developed to predict the mechanical response of the honeycomb insole, namely an *Explicit model* and a *Homogenized model* using *Abaqus* (version 6.14) commercial

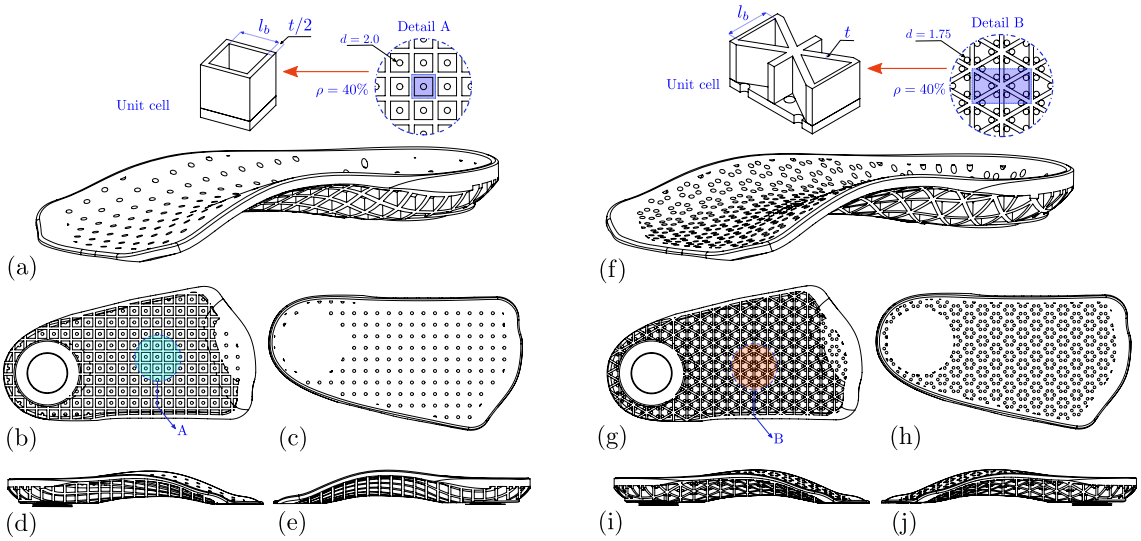

Figure 4: Geometrical details of the designed square and triangular lattice FOs; (a) isometric view, (b) bottom view, (c) top view, (d) left view and (e) right view of the square lattice FO; (f) isometric view, (g) bottom view, (h) top view, (i) left view and (j) right view of the triangular lattice FO. The dimensions are in mm and the relative density of the cells is 40%. The holes at the first layer have different diameters and patterns when compared to the honeycomb lattice FO design. Correspondingly, their first layer have a different effective properties. These two lattice insoles were designed to study the effect of the cell topology on the predictive capability of their homogenized models.

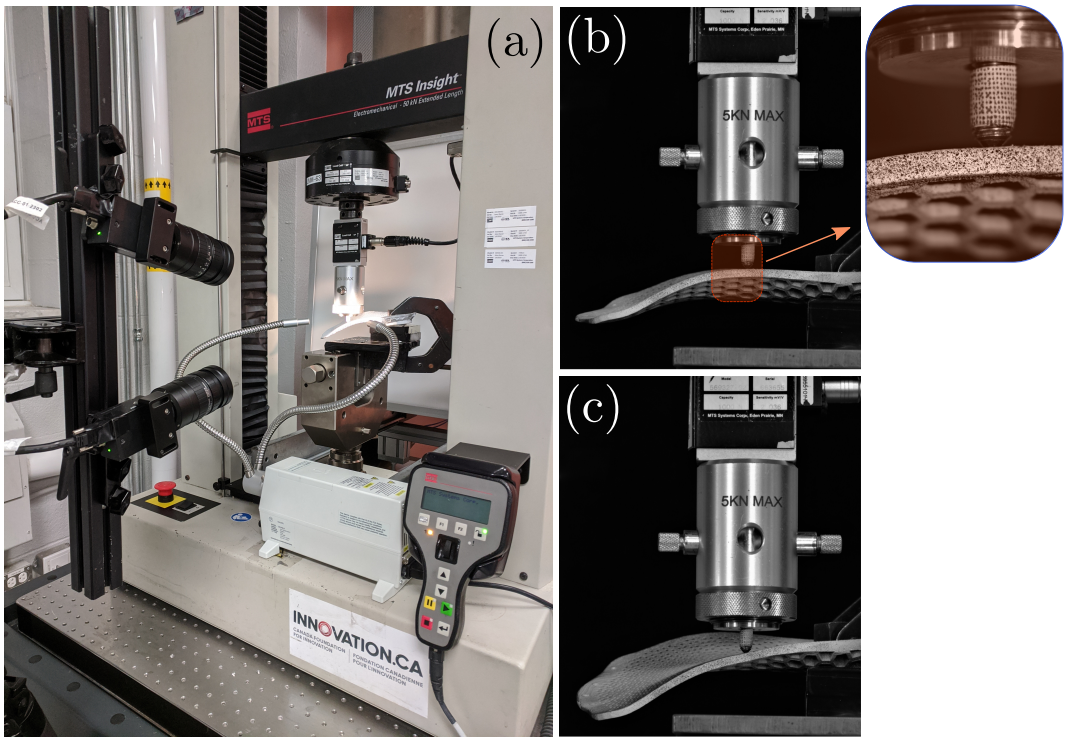

Figure 5: Experimental setup to apply a displacement over the longitudinal arch of the 3D printed insole and measure the reaction force; (a) the painted insole is under a compression loading using a MTS uni-axial tensile machine in front of two cameras, (b) the insole before load application, (c) the insole after load application. The machine applied a vertical displacement and a 1 kN load cell recorded the reaction force over the punch. The punch was an `M6` screw that was mounted into the fixture. The insole was fixed at the heel part using a C-clamp. The cameras were mounted on a tripod, placed close to the specimen and a 10 mm lens extension was employed to have a higher resolution. An *LED-Olympus LG-PS2* Microscope Ring Light was also employed to control the lighting.

FE software. In the explicit model, the geometry was explicitly meshed by 3D elements whose mechanical properties were considered as isotropic and linearly elastic with the measured Young's modulus and Poisson's ratio during the tensile test. In the homogenized model, on the other hand, the geometry was meshed by shell elements whose mechanical properties were computed from the numerical homogenization process.

3.3.1 Numerical homogenization process

Numerical homogenization was employed to compute the effective properties of the unit cell in Figure 3. The microstructure is periodic in-plane but is not periodic out-of-plane. This causes a challenge because the numerical homogenization technique requires 3D periodic micro-structures. To circumvent this problem, we relied on the classical lamination theory to assemble two layers made of a homogenized layer with a distribution of circular holes and a layer consisting of the homogenized mechanical properties of the honeycomb cell (see

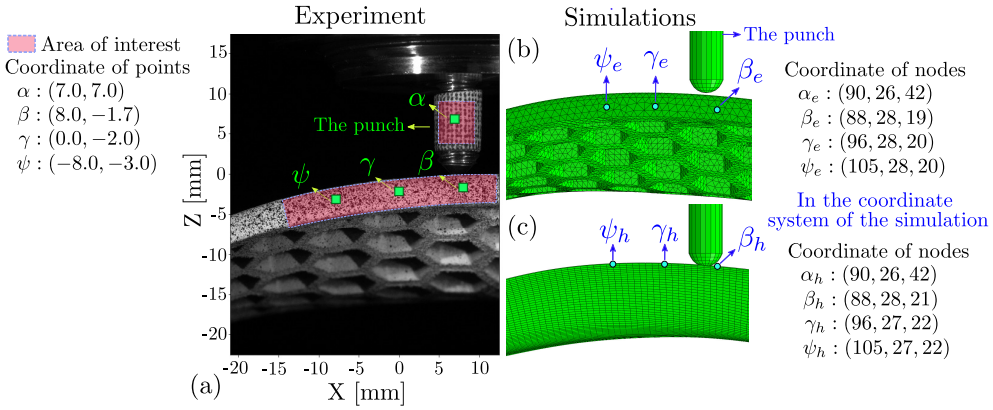

Figure 6: The selected points for validating the predicted vertical displacement field by the models; (a) the area of interest and selected points in the digital image correlation measurement, (b) the corresponding selected nodes over the explicit FE model, (c) the selected nodes over the homogenized FE model.

Figure 3(c)). The numerical homogenization computes the effective stiffness tensor of the layer with holes and the layer with honeycomb namely as $\bar{C}^{\text{Hole}}_{ijkl}$ and $\bar{C}^{\text{Honeycomb}}_{ijkl}$, respectively. A Python code was written to automatically generate, mesh, apply PBC, apply strain tensors, and compute the effective properties of the unit cells as a function of the geometrical parameters described in Section 3.1. Particularly, the effective properties were computed for honeycomb cells having relative densities of $\rho = 10\%, 20\%, 30\%, 40\%, 50\%, 60\%, 70\%$ and 80%. The same relative densities were also used to compute the square and triangular cells effective properties. The effective properties were reported as the engineering constants (*i.e.*, $E_{11}, E_{22}, E_{33}, G_{12}, G_{13}, G_{23}, \nu_{12}, \nu_{13}$, and ν_{32}) since all the cells have three symmetrical planes and are orthotropic. The computed effective properties were injected to a shell FE model with a variable thickness.

3.3.2 Modelling of the variable thickness

The height of h_2 was a variable in our designed FO. Figure 7(a) shows the distribution of h_2 with respect to $X - Y$ in-plane coordinate system attached to the insole. The CAD file of the insole was meshed and the Z coordinate of nodes at the top (Z_{Top}) and bottom (Z_{Bottom}) surfaces of the FO were used to compute h_2. In this way, $h_1 + h_2 = Z_{Top} - Z_{Bottom}$. Assuming that h_1 is constant, h_2 is simply computed by $h_2(X, Y) = Z_{Top} - Z_{Bottom} - h_1$. To simulate this variable thickness, the homogenized model was divided into $n_x \times n_y$ segments. The segmentation was conducted using vertical (in direction of Y) and horizontal planes (in direction of X). Each segment was assigned to a mean value of h_2 in the corresponding domain. Figure 7 shows our discretization of h_2 when the segment size was $\Delta_x = \Delta_y = 24$ mm. The appendix A shows the numerical stability of such discretization scheme for more segment sizes.

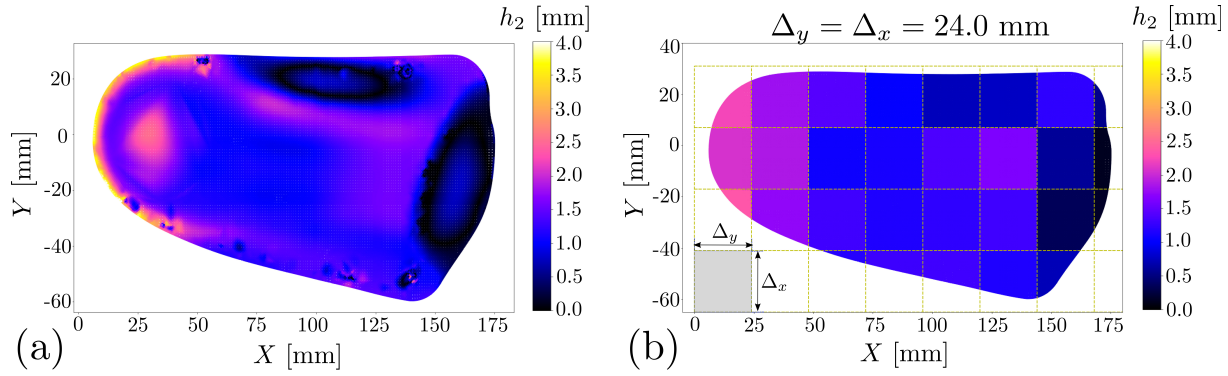

Figure 7: Modelling of variable height h_2; (a) the reference distribution of $h_2(X, Y)$ over the explicit model of the insole, (b) the discretized distribution of $h_2(X, Y)$ over the homogenized model of the insole by $\Delta_x = \Delta_y = 24.0$ mm.

3.3.3 Simulation of insole under static pressure distribution

The simulation of the insole under the static pressure distribution of the foot was conducted to assess the predictive capability of the homogenized model when compared to the predictions of the explicit model. In both models, the heel part of the insole was assumed to be fixed in all degrees of freedom, and the forefoot part was fixed in the vertical direction. The static pressure distribution of the foot (*i.e.*, $P(X, Y)$) was then directly applied over the top surface (*i.e.*, the surface that is in contact with the foot) of the models. Figure 8 shows how the loading and the boundary conditions were applied over the FE model of the insole. In this Figure, part (a) shows the pressure distribution at 50% of the stance phase that was selected to be applied over the nodes at the top surface of the FE models. This pressure was measured through a continuous surface of the pressure sensor. The FO's top surface, however, is not continuous and has circular holes. This leads to a mismatch between the applied total force ($F_t = P \times A$) over the explicit model and the homogenized model since the area of the top surface having circular holes is $A_1 = 110\ cm^2$, and without holes, is $A_2 = 130\ cm^2$. Therefore, the applied pressure distribution over the explicit model was scaled up by the factor $A_2/A_1 = 1.18$ to ensure that loading in both FE models are equivalent. The same pressure distribution having scaling factors of $A_2/A_1 = 130/120 = 1.08$ and $A_2/A_1 = 130/110 = 1.18$ was applied over the square and triangular cells, respectively. Note that the foot pressure distribution was particularly measured for honeycomb lattice insole and changing the cell topology changes the insole's rigidity and it would affect the foot pressure distribution within the gait [32]. However, from a verification point of view, as far as the loading and the boundary conditions are the identical for both the explicit and the homogenized models, they should predict the same mechanical response and thus the comparison of their predictions is still valid.

In Figure 8 (b), the boundary conditions at the heel part were applied in a circular zone having its center at $(34.31, -2.06)$ mm. In the full meshed model, the radius is 10.5 mm to fix the three translations of U_X, U_Y and U_Z. In the homogenized model, the radius is 13.25 mm to fix the three translations (*i.e.*, $U_X = U_Y = U_Z = 0$) and two in-plane rotations (*i.e.*, $R_X = R_Z = 0$). The difference between the selected radius comes from the geometrical

details of the insole at the heel part (see Figure 2). In the forefoot, a circular zone having its center located at $(195.0, -20.0)$ mm and a radius of 52.0 mm was selected to fix only the out-of-plane translation U_Z. These boundary conditions of course are not accurately representative of the interactions of insoles between the shoes and the feet. It was employed only for the purpose of the verification of the homogenized model's predictions.

The verification consisted in comparing the displacement field in direction of Z over the nodes at the top surface of the explicit model, as well as the top surface of the homogenized model of the lattice insole. The predictions were also compared over three vertical and three horizontal lines, as shown in Figure 9. In all six lines, the relative discrepancy of the homogenized model's prediction against the explicit model was reported to evaluate the homogenized model's performance assuming that the explicit model's prediction is the reference solution. The evaluation metric was defined as $\delta = \left| \frac{\max |U_Z^{\mathrm{E}}| - \max |U_Z^{\mathrm{Hmg}}|}{||U_Z^{\mathrm{E}}||_2} \right|$ which is the relative difference between the maximum absolute values of the predictions normalized by the norm-2 of the reference solution. This metric was selected since it was expected that the homogenized model, as the surrogate, predicts well the maximum vertical displacement within an optimization problem.

The computational costs of the simulations were then compared within a convergence study of mesh refinement. The mesh of both FE models was uniformly refined as $\frac{l_{\mathrm{element}}}{l_b} = 3, \frac{3}{2}, 1, \frac{1}{2}, \frac{1}{3}, \frac{1}{4}, \frac{1}{5}, \ldots$. The refinement was stopped when:

$$\bar{\Delta} U_{Z\min} = \frac{U_{Z\min}^{\mathrm{fine}} - U_{Z\min}^{\mathrm{coarse}}}{U_{Z\min}^{\mathrm{fine}}} \leq 0.001, \tag{5}$$

where $\bar{\Delta} U_{Z\min}$ returns the normalized difference between the predicted minimum out-of-plane displacement having a fine mesh ($U_{Z\min}^{\mathrm{fine}}$) against the predicted one by a coarse mesh ($U_{Z\min}^{\mathrm{coarse}}$). The required memory and the computational time to provide the converged result were reported to compare the computational efficiency of the explicit model against the homogenized model.

3.3.4 Simulation of foot orthotic under a concentrated force

The simulation of the FO under the concentrated force was a contact simulation. The geometry of the punch was approximately defined in Abaqus. A fillet radius of 2.5 mm was added into the geometry of the punch to avoid numerical issues due to the contact problem between a sharp edge and the insole's surface. The center of the cylindrical punch was placed close to the edge of the insole at coordinates $(89.75, 25.5, 41.2)$ mm. The punch was assumed to be an analytical rigid body since the steel punch was much stiffer than the polymeric 3D printed insole (*i.e.*, $\frac{E_{steel}}{E_{insole}} \approx \frac{200\mathrm{GP}}{2GP} = 100$). To apply the displacement over the punch, one *Reference Point* was defined at the top and the center of the punch. A rigid constrain was then defined between the reference point and the surface of the punch. The normal contact behaviour was defined as *Hard Contact* and the tangential contact behaviour was defined as *Frictionless* between the punch and the insole's top surface. In this interaction, the *master element* was the punch and the *slave element* was the top surface of the insole. Next, the

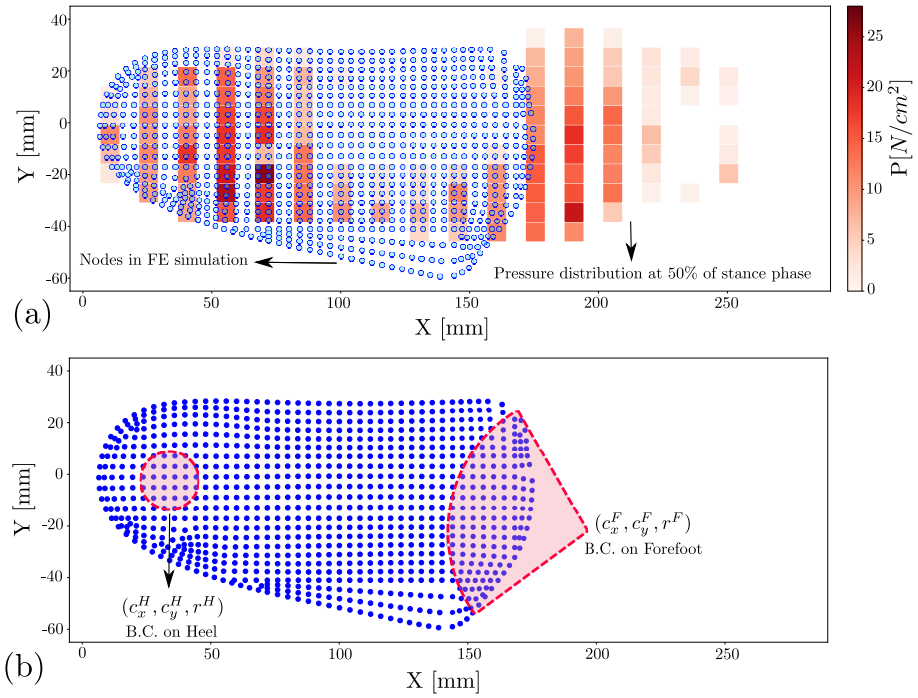

Figure 8: Loading and boundary conditions over the FE simulation of the insole; (a) applying the measured pressure distribution of right foot at 50% of the stance phase (midstance) over the FE model of the insole in the same coordinate system as the FE simulation. Note that the pressure values of lower than 0.5 N/cm^2 have been neglected in this presented pressure contour; (b) applied boundary conditions on the heel and forefoot parts of the insole withing a circular zone with center's coordinate and radius of (c_x^H, c_y^H, r^H) and (c_x^F, c_y^F, r^F), respectively. At the heel part, all degrees of freedom were fixed and at the forefoot, only the out-of-plane translation was fixed (*i.e.*, $U_Z = 0$).

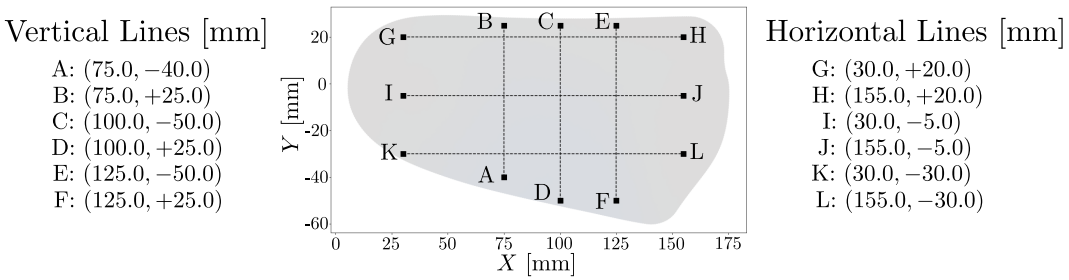

Figure 9: Selected lines to compare the predicted U_Z by the explicit and the homogenized models in the FE simulation of the insole under the foot pressure.

vertical displacement was applied at the reference point with a value of $U_Z = 15.0$ mm while the other five degrees of freedom of the reference point were considered to be fixed to 0. As a result, the vertical reaction force over the punch was computed at the reference point and plotted as a function of the reference point's vertical displacement for the purpose of validation against the experimentally measured force-displacement curve.

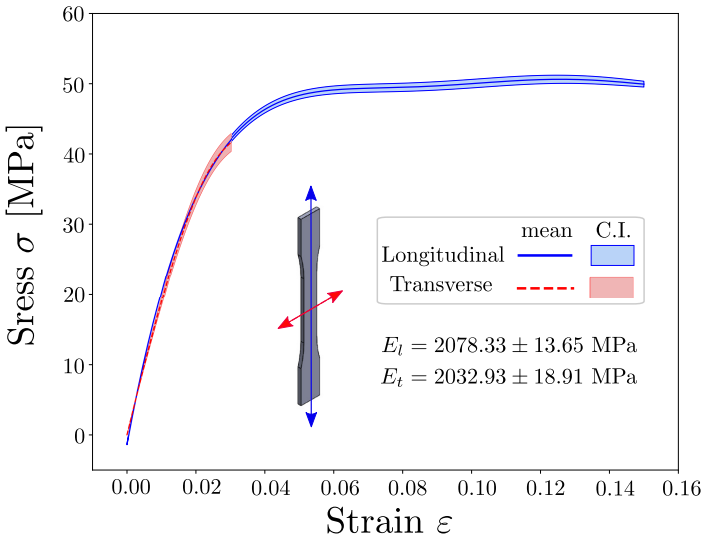

Figure 10: The experimentally measured stress-strain curve over the 3D printed Nylon-12 dog-bone specimens submitted to a uni-axial tensile test. The stress is the *nominal* stress which is computed by the measured reaction force divided by the cross-section area. The strain is the *Green-Lagrangian* strain which was computed by *Vic-3D*. The dog-bones were type `I` according to `ASTM-D638` standard. The printing orientations included longitudinal and transverse directions. The computed Young's modulus over these two types were almost the same having relative difference smaller than 3%. The Young's modulus, therefore, was assumed to be constant and equal to $E = 2\ 056$ MPa.

4 Results and Discussion

4.1 Stress-Strain curve of dog-bone specimens

Figure 10 shows the stress-strain curves of the tested dog-bone specimens submitted to the tensile test. The curves correspond to the means of the measured axial stress and strain at the center point of the specimens, along with 90% confidence intervals that are computed from a t-distribution of five specimens for longitudinal and transverse 3D printing orientations. The material reveals a nonlinear behaviour after $\varepsilon \approx 0.015$ with the yield stress of $\sigma_y \approx 28$ MPa. In the linearly elastic domain, the Young's modulus of the specimens with longitudinal and transverse 3D printing orientations were extracted as $E_l = 2\ 078 \pm 14$ and $E_t = 2\ 033 \pm 19$ MPa, respectively. The relative difference between E_t and E_l is 2.18%. Assuming that $E_t \approx E_l$, the average value of $E = 2\ 056$ MPa was injected into the numerical simulations. Moreover, it was assumed that $\nu_t \approx \nu_l$, and the average Poisson's ratio was computed as $\nu = 0.37$ at the center point of the dog-bone specimens using the extracted strain fields of ε_{xx} and ε_{yy} by DIC.

4.2 Effective mechanical properties for the unit cell

Table 1 reports the computed effective properties of the unit cells, when the material's elastic properties are $E = 2\ 056$ MPa and $\nu = 0.37$. Here, the relative density of the honeycomb cell is 40%. These effective properties have been verified and validated by the authors in [33]. The relative density of its corresponding layer with circular holes is 96%. As a result, its effective properties are close to the bulk material properties. Table 1 also reports the computed effective properties of square and triangular cells having the same relative density of 40%, as well as the effective properties of their layers with holes. Moreover, Figure 11 shows the computed effective properties of the three cells as a function of the relative density. Depending on the required stiffness, the proper cell topology, as well as its relative density, could be selected from these curves.

Table 1: The effective proprieties of the honeycomb, triangular and square lattice insoles.

Property	Hc.	Tr.	Sq.	$\text{Holes}^{\text{Hc.}}$	$\text{Holes}^{\text{Tr.}}$	$\text{Holes}^{\text{Sq.}}$
$\bar{E}_{11}$ (MPa)	231	369	512	1823	1574	1838
$\bar{E}_{22}$ (MPa)	231	367	511	1823	1572	1757
$\bar{E}_{33}$ (MPa)	817	822	821	1965	1851	2001
$\bar{G}_{12}$ (MPa)	73	141	18	673	586	587
$\bar{G}_{13}$ (MPa)	183	177	181	686	614	633
$\bar{G}_{23}$ (MPa)	183	177	181	686	614	632
ν_{12}	0.58	0.30	0.06	0.36	0.35	036
ν_{13}	0.10	0.17	0.23	0.34	0.31	0.31
ν_{23}	0.10	0.17	0.23	0.34	0.31	0.35

4.3 Simulation of insole under static pressure distribution

4.3.1 Convergence study of the explicit and the homogenized models

Figure 12 shows the convergence and the required memory of the explicit model, as well as the homogenized model, to predict the minimum out-of-plane displacement of the honeycomb insole having a relative density of $\rho = 40\%$ and under the pressure distribution of the foot. In the explicit model's convergence study, the mesh size were of $\frac{l_{\text{element}}}{l_b} = 3, \frac{3}{2}, 1, \frac{1}{2}, \frac{1}{3}, \frac{1}{4}, \frac{1}{5}$ and $\frac{1}{6}$ with a uniform mesh refinement. In the homogenized model's convergence study, the mesh size were of $\frac{l_{\text{element}}}{l_b} = 3, \frac{3}{2}, 1, \frac{1}{2}, \frac{1}{3}, \frac{1}{4}, \frac{1}{5}, \frac{1}{6}$ and $\frac{1}{7}$. When considering the convergence criterion of Equation 5, the accepted mesh size for the explicit model is $\frac{1}{6}$, which results approximately in 10^6 solid elements and 4.68×10^6 DOFs, while, for the homogenized model, the accepted mesh size is $\frac{1}{7}$ which results in 3.7×10^4 shell elements and 9×10^5 DOFs. The required memory to obtain the converged results by the explicit model is 4 280 MB. The total CPU time to accomplish this converged simulation is 2 149 seconds on a personal computer

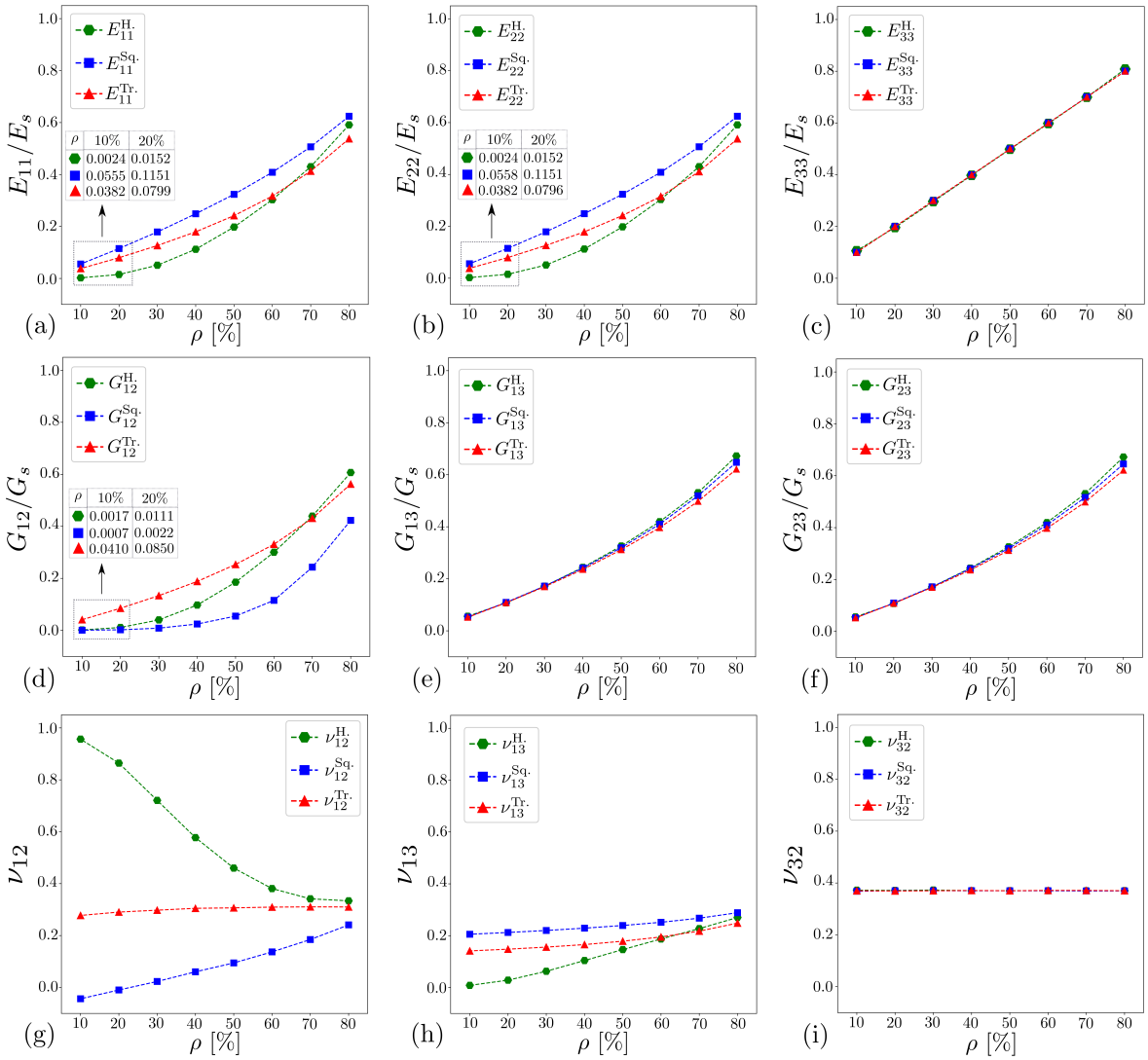

Figure 11: Computed effective properties of honeycomb, square and triangular cells with respect to the relative density; (a) E_{11}/E_s, (b) E_{22}/E_s, (c) E_{33}/E_s, (d) G_{12}/G_s, (e) G_{13}/G_s, (f) G_{23}/G_s (g) ν_{12}, (h) ν_{13} and (i) ν_{32}. The effective properties were computed particularly for $\rho = \{10\%, 20\%, 30\%, 40\%, 50\%, 60\%, 70\%, 80\%\}$. Except for the Poisson's ratios, the computed elastic constants are normalized with the bulk properties E_s and G_s.

featuring an Intel® Core™ i7-8700K CPU @ 3.7 GHz and 64 GB RAM. In the homogenized model, on the other hand, employing 464 MB memory yields the converged results in which the total CPU time is 47 seconds. Therefore, in this simulation, the homogenized model is almost 9 times more efficient and 46 times faster than the explicit model in terms of the required memory and the computational time, respectively.

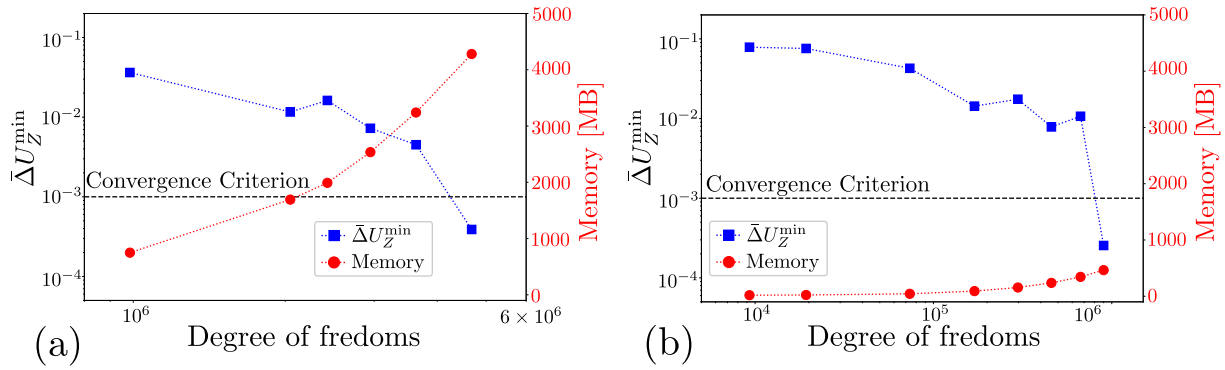

Figure 12: Mesh size convergence study for (a) the explicit model and (b) the homogenized model under the pressure distribution of the foot. The Figure also shows the minimum required memory to conduct the FE simulations using Abaqus. The explicit model needs 4 280 MB to predict the converged results while the homogenized model only requires 464 MB to return the converged result according to the convergence criterion of Equation 5. Consequently, the total CPU time for the explicit model was 2 149 seconds while it was 47 seconds (*i.e.* 46 times faster) for the homogenized model using a personal computer featuring Intel® Core™ i7-8700K CPU @ 3.7 GHz and 64 GB RAM.

4.3.2 Comparing the predictions of the explicit and homogenized models

Figure 13 shows a comparison between the performance of the explicit model and homogenized model to predict the vertical displacement U_Z of the honeycomb insole having a relative density of 40% under the foot pressure distribution and boundary conditions of Figure 8. In Figure 13, part (a) shows the predicted U_Z by the explicit model, part (b) shows the predicted U_Z by the homogenized model and part (c) shows the computed relative difference at each point normalized by the maximum predicted displacement by the explicit model (*i.e.*, $\frac{|U_Z^{\mathrm{E}} - U_Z^{\mathrm{Hmg}}|}{\max |U_Z^{\mathrm{E}}|}$). To compute this difference, the predicted nodal displacements of the explicit model were interpolated using cubic interpolation into the same coordinate nodes of the homogenized model. This result shows that the maximum value of this relative difference is 29%. The discrepancy is higher around the applied boundary conditions at forefoot and near the edge (*i.e.* $110.0 \leq X \leq 150.0$ mm and $-60.0 \leq Y \leq -40.0$ mm). This error might be due to the fact that the homogenized model relies on a structure having an infinite number of cells and thus it does not account for edge effects. Nevertheless, the homogenized model, as a surrogate, is able to approximately predict the same local minimum or maximum displacement, when compared to the predictions of the explicit model. For instance, Figure 14 shows the predicted U_Z by the two models along three vertical and three horizontal lines between points (A, B), (C, D), (E, F), (G, H), (I, J) and (K, L) over the top surface of the insole. Among them, the highest discrepancy is 7.85% to predict the local minimum displacement U_Z within the line (G, H).

Figures 15, 16, 17 and 18 report the evaluation of the homogenized model's performance to predict the displacement U_Z of the square and triangle cellular insoles submitted to the same foot pressure distribution and boundary conditions as shown in Figure 8. In

both cases, the homogenized model is able to predict the local minima within the lines (G, H), (I, J) and (K, L). The maximum normalized relative difference is $\delta = 13.71\%$ for the homogenized square insole and it is $\delta = 14.47\%$ for the homogenized triangular insole. The average discrepancies among the lines ($\bar{\delta}$) are $\bar{\delta}^{\text{Hc.}} = 2.55\%$, $\bar{\delta}^{\text{Sq.}} = 4.25\%$ and $\bar{\delta}^{\text{Tr.}} = 5.15\%$ for honeycomb, square and triangular cells, respectively. This shows a lower predictive capability of the homogenized square insole and the homogenized triangular insole, when compared to the homogenized honeycomb insole. The difference may come from a higher stress concentration factor in the corners of square and triangular geometries, when compared to the hexagonal geometry [34]. In the homogenization process of square and triangular cells, the effective properties were overestimated and the homogenized model, correspondingly, is not able to accurately capture the displacement field and overestimates the structure's rigidity. Besides modelling, in the manufacturing of square or triangular lattice insoles, the stress concentration at the corners might be a reason to start the crack propagation [35]. Moreover, the insole is under repeated bending and/or torsion during walking cycles and fatigue fracture thus might occur from these critical points. This implies the necessity of considering fillet radius at the corners to release the stress concentration in these cells [36, 37]. Otherwise, among these three lattices, the recommended design is the honeycomb lattice insole.

4.4 Simulation of insole under contact force

4.4.1 Validation of the predicted force-displacement curves

Figure 19 shows the experimentally measured force-displacement curve as well as the predicted forces by the homogenized model and the explicit model of the honeycomb FO having a relative density of 40%. The experimental force corresponds to the mean of three repetitions of the test at the same loading point and by re-installation of the clamped boundary condition. The predicted forces come from the reaction forces at the reference points in the explicit and the homogenized models. The normalized relative difference between the measured force and that predicted is computed by $||F^{\text{Experiment}} - F^{\text{model}}||_2/||F^{\text{Experiment}}||_2$. In this way, the relative difference between the explicit model's prediction against the average experimentally measured force-displacement curve is 9.77% and for the homogenized model's prediction, it is 9.27%. The relative difference between the predictions of the homogenized model and the explicit model is less than 1%. This result, therefore, confirms that the explicit model's prediction can be replaced by the homogenized model's prediction to reduce the computational cost in a contact simulation.

In this simulation, the required memory to run the explicit model in each time increment is 3 578 MB while it is only 213 MB for the homogenized model. The required memory thus is reduced by 94% in the homogenized model. Moreover, the homogenized model is more efficient in terms of the number of iterations to reach convergence. There are 791 iterations to complete the explicit model simulation, and, on the other hand, there are 276 iterations for the homogenized model. Consequently, the computational time for the explicit model is 78 184 seconds (*i.e.*, almost 22 hours), while it is 1 298 seconds (*i.e.*, almost 22 minutes) for the homogenized model using 12 processors in a parallel processing of Abaqus analysis on a computer featuring an Intel® Core™ i7-8700K CPU @ 3.7 GHz and 64 GB RAM.

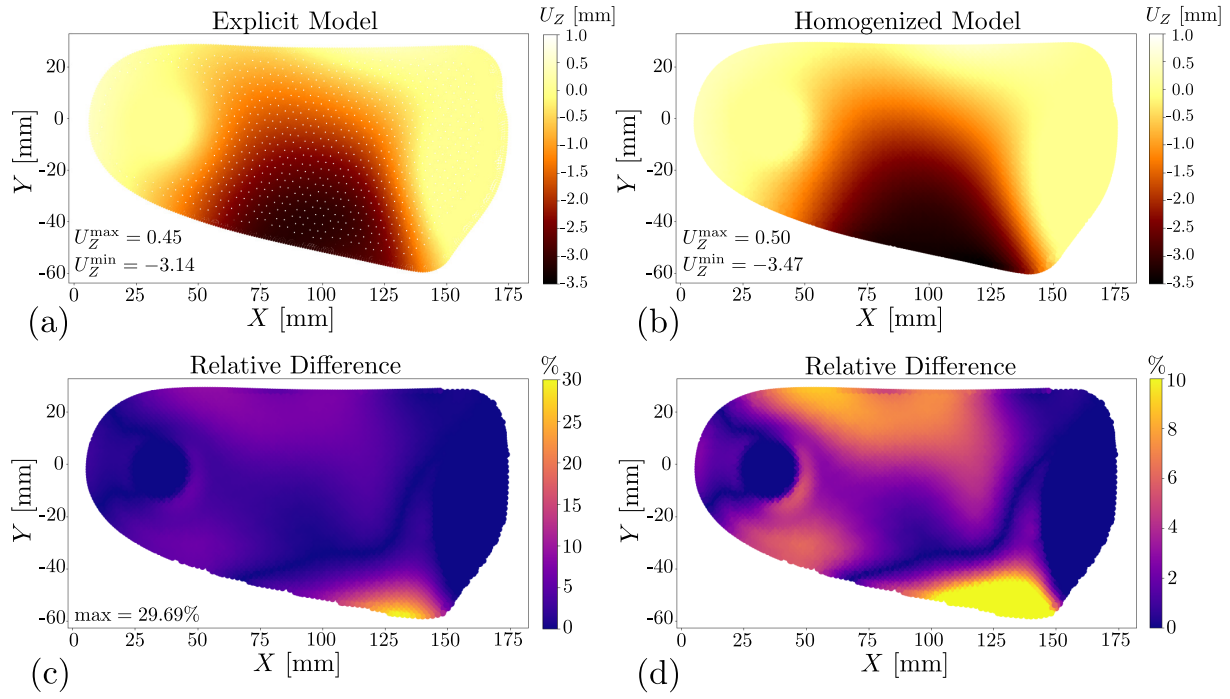

Figure 13: Evaluation of the predictive capability of the homogenized model for the honeycomb lattice insole, when compared to the prediction of the explicit model as the reference solution; (a) The predicted U_Z by the explicit model, (b) the predicted U_Z by the homogenized model, (c) the computed relative difference between the predictions of both models and normalized by the maximum predicted displacement by the explicit model ($\frac{|U_Z^{\mathrm{E}} - U_Z^{\mathrm{Hmg}}|}{\max |U_Z^{\mathrm{E}}|}$), (d) The computed relative difference having a range of $0 - 10\%$ to better show its variation. The maximum discrepancy in figure (c) is 29.69%, which is close to the applied boundary conditions and may come from the edge effect.

4.4.2 Validation of the predicted displacement field

Figure 20 shows the experimentally measured and the predicted displacement field U_Z by the explicit and the homogenized models of the honeycomb FO. The displacement fields are presented at five time frames during the load history having applied displacements of $D = 4, 6, 8, 10$ and 12 mm over the punch. Figure 21 quantitatively shows the measured and predicted displacements at three points of β, γ and ψ with respect to the displacement of the punch at point α. In this comparison, the normalized relative difference between the measured displacement and that predicted is computed by $||U_Z^{\mathrm{Experiment}} - U_Z^{\mathrm{model}}||_2 / ||U_Z^{\mathrm{Experiment}}||_2$. In this way, the discrepancy of the explicit model is 6.32%, 6.28%, 5.67%, and for the homogenized model is 4.16%, 4.25% and 4.33% over the points β, γ and ψ, respectively.

4.4.3 Contribution factors to the variability of measurements

The uncertainty of the experiment mainly comes from variability of measurements. To quantify this variability, Figure 22 shows the average measured displacements by the MTS machine and the DIC within three repetitions. The DIC displacement was extracted at

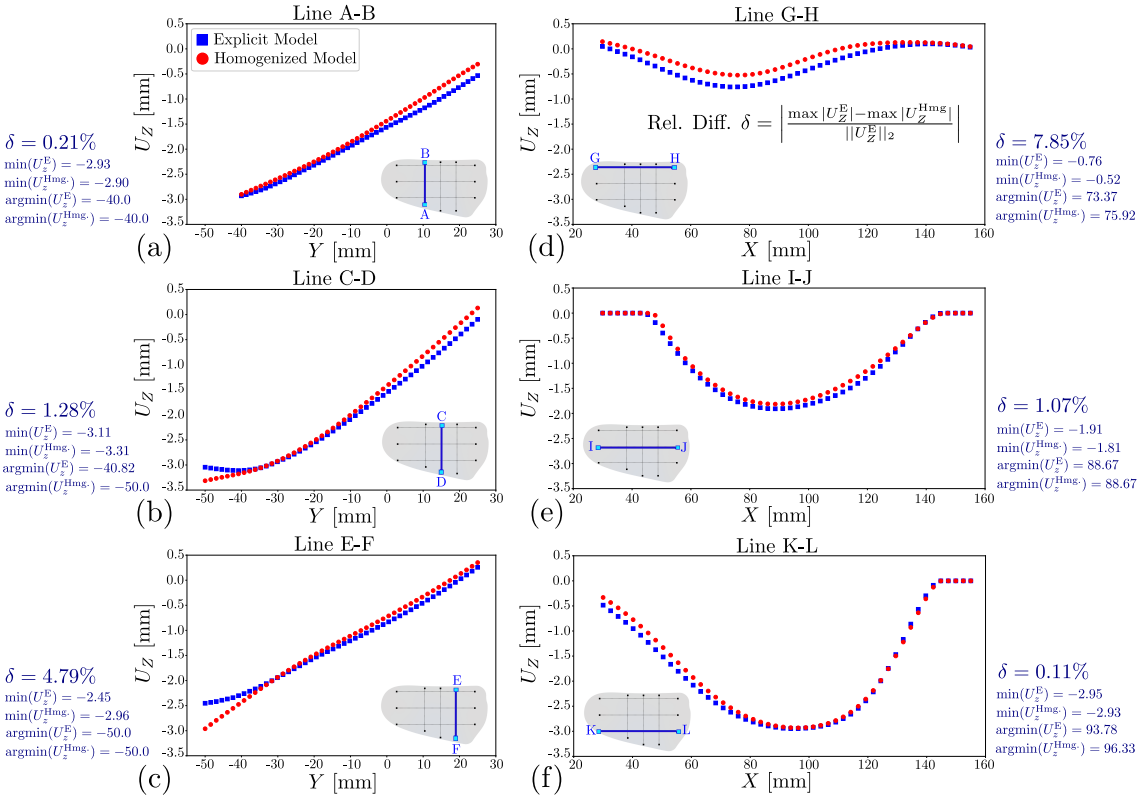

Figure 14: Comparison of the predicted displacement U_Z by the explicit model as well as the homogenized model for the honeycomb lattice insole at; lines (a) (A, B), (b) (C, D), (c) (E, F), (d) (G, H), (e) (I, J) and (f) (K, L). The metric δ represents the discrepancy of the homogenized model to predict the minimum displacement when compared to the predictions of the explicit model. This metric shows that the maximum discrepancy of the homogenized model is 7.85% in line (G, H) (*i.e.*, the medial arch) among the selected lines. This level of accuracy could be acceptable for the optimization application.

point α over the punch. The MTS displacement was received from the machine which represents the vertical translation of the upper fixture (see also Figure 5). In this measurement, the inaccuracy thus mainly comes from the mismatches and looseness between the body components (frame, fixture, punch, ...) and of course the finite machine precision. In this experiment, the force acting on the system is small (less than 0.5 kN) and this variability is not probably significant. The inaccuracy in DIC measurement comes from the calibration error and the projection error. In this test, the calibration error is 0.074 and the projection errors for each of the repetitions are 0.0628, 0.0579 and 0.0763. Yet, both calibration and projection errors are accepted according to the VIC3D software. Moreover, in general, as Figure 22 shows, these two measurements are very close to each other (having a normalized relative difference of $||D^{\mathrm{MTS}} - D^{\mathrm{DIC}}||_2 / ||D^{\mathrm{MTS}}||_2 = 1.02\%$). Both measurements, therefore, could be acceptable for the purpose of the validation of the simulation's predictions.

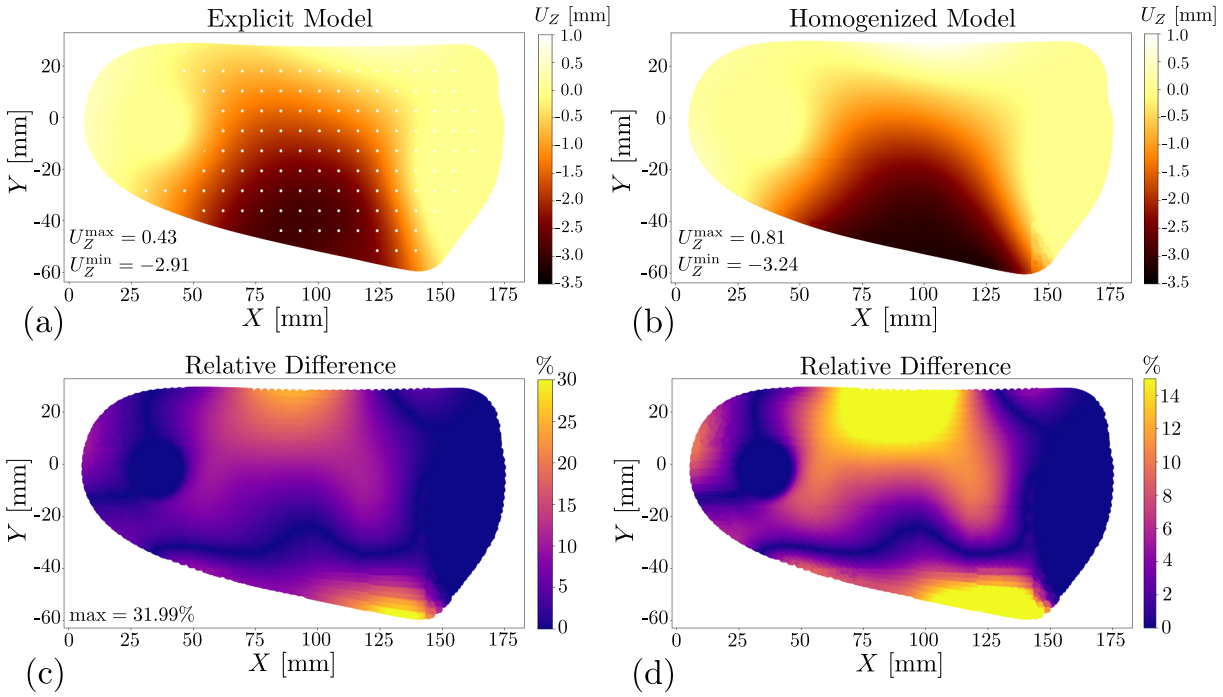

Figure 15: Evaluation of the predictive capability of the homogenized model for the square insole, when compared to the prediction of the explicit model as the reference solution; (a) The predicted U_Z by the explicit model, (b) the predicted U_Z by the homogenized model, (c) the computed relative difference between the predictions of both models and normalized by the maximum predicted displacement by the explicit model ($\frac{|U_Z^{\mathrm{E}} - U_Z^{\mathrm{Hmg}}|}{\max |U_Z^{\mathrm{E}}|}$), (d) The computed relative difference having a range of $0 - 15\%$ to better show its variation. The maximum discrepancy in figure (c) is 31.99%, which is close to the applied boundary conditions and may come from the edge effect.

5 Conclusion

We developed a computationally efficient FE model of a honeycomb lattice foot orthotic. The contributions and conclusions of this modelling are as follows:

- In a FE simulation of a honeycomb lattice FO under static pressure distribution of the foot, the required memory to run the homogenized model is 9 times smaller than the required memory for the explicit FE model. The computational time of the homogenized model is 46 times faster than the explicit model. Yet, the relative difference between their predictions is less than 8% to predict the local minimum out-of-plane displacement within the selected vertical and horizontal lines over the top surface of the insole. Each line could be a potential target in an optimization problem to control the deformation of FO by changing the cell's geometrical parameters.

- For the explicit model, changing the cell's geometrical parameters requires modifying the CAD file and correspondingly re-meshing the lattice FO which is an elaborate task during each iteration of the optimization process. For the homogenized model,

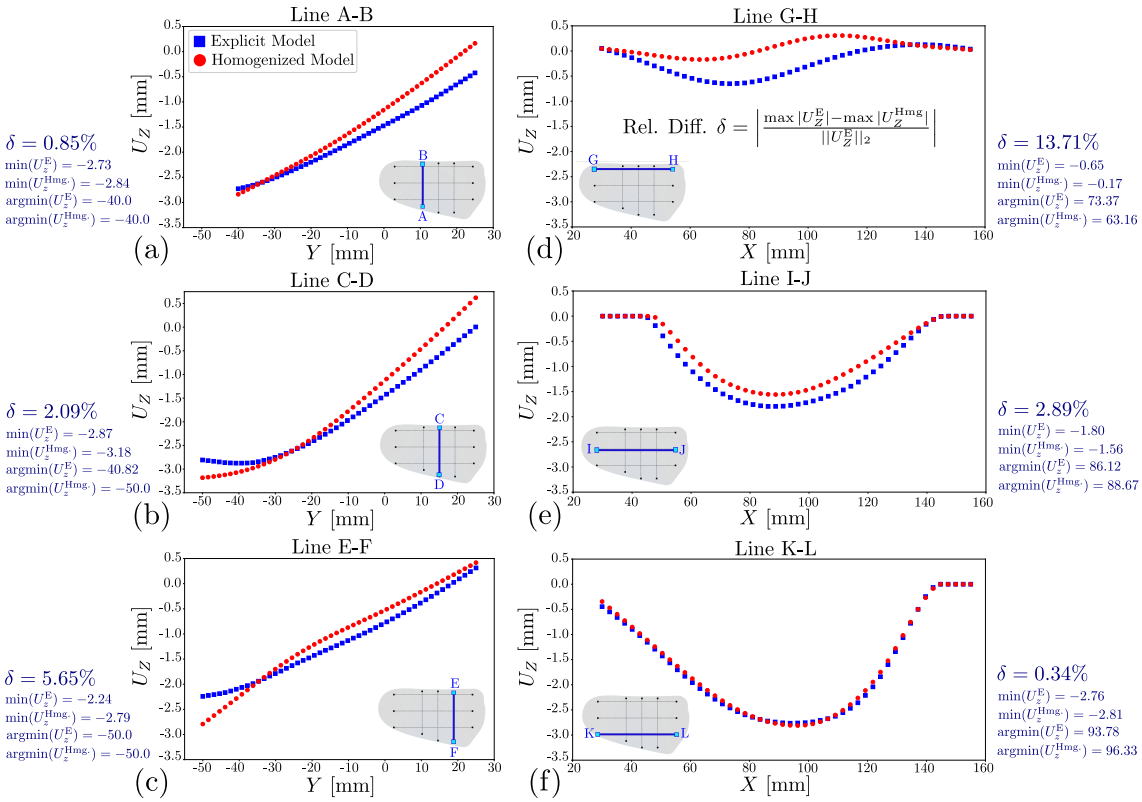

Figure 16: Comparison of the predicted displacement U_Z by the explicit model as well as the homogenized model for the square lattice insole at; lines (a) (A, B), (b) (C, D), (c) (E, F), (d) (G, H), (e) (I, J) and (f) (K, L). The metric δ represents the discrepancy of the homogenized model to predict the minimum displacement when compared to the predictions of the explicit model. This metric shows that the maximum discrepancy of the homogenized model is 13.71% in line (G, H) (*i.e.*, the medial arch) among the selected lines.

on the other hand, it is sufficient to change the effective properties (and/or the shell's thickness) and there is no need to change the mesh.

- In a contact simulation, the homogenized model yields approximately the same reaction force as the explicit model having a relative difference of less than 1%. Both models predict a contact force with a relative difference of less than 10% when compared to the experimentally measured force-displacement curve. But, the explicit model takes 22 hours to run while the homogenized model takes 22 minutes using a personal computer with an Intel® Core™ i7-8700K CPU @ 3.7 GHz and 64 GB RAM.

- The predictive capability of the homogenized model is affected by the cell topology. The maximum discrepancy of the homogenized model displacement with respect to the explicit model displacement (*i.e.*, δ) for the square lattice insole is 13.71% and for the triangular lattice insole is 14.47%. These homogenized models might be still functional since they are able to approximately provide the local minimum displacement.

The presented homogenized models, therefore, can be employed as a surrogate to accel-

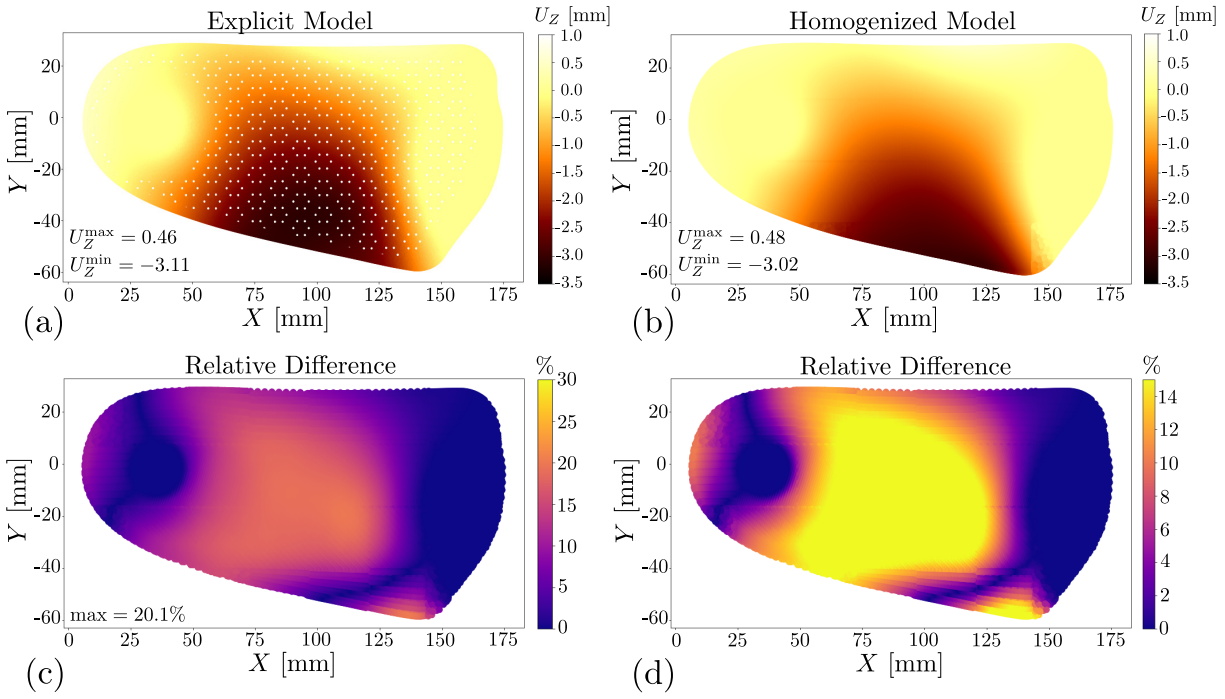

Figure 17: Evaluation of the predictive capability of the homogenized model for the triangular lattice insole when compared to the prediction of the explicit model as the reference solution; (a) The predicted U_Z by the explicit model, (b) the predicted U_Z by the homogenized model, (c) the computed relative difference between the predictions of both models and normalized by the maximum predicted displacement by the explicit model ($\frac{|U_Z^{\mathrm{E}} - U_Z^{\mathrm{Hmg}}|}{\max |U_Z^{\mathrm{E}}|}$), (d) The computed relative difference having a range of $0 - 15\%$ to better show its variation. The maximum discrepancy in figure (c) is 20.1%.

erate the optimization process of the lattice FOs for a given cost function. Alternatively, it could be used in a complex biomechanical system including the foot topology and the cellular FO to speed up the computational time and the convergence rate.

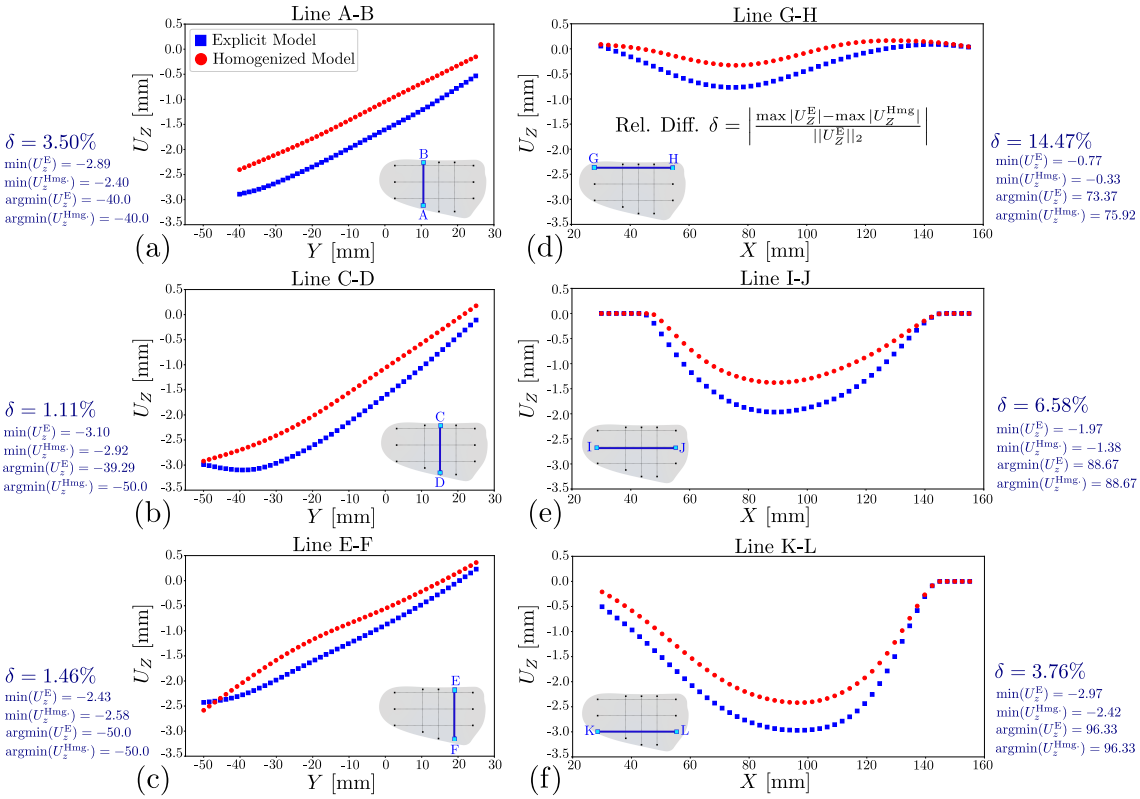

Figure 18: Comparison of the predicted displacement U_Z by the explicit model as well as the homogenized model for the triangular lattice insole at; lines (a) (A, B), (b) (C, D), (c) (E, F), (d) (G, H), (e) (I, J) and (f) (K, L). The metric δ represents the discrepancy of the homogenized model to predict the minimum displacement when compared to the predictions of the explicit model. This metric shows that the maximum discrepancy of the homogenized model is 14.47% in line (G, H) (*i.e.*, the medial arch) among the selected lines.

6 Declaration of competing interest

The authors declare that they have no known competing financial interests or personal relationships that could have appeared to influence the work reported in this paper.

7 CRediT author statement

Mohammadreza Moeini: Conceptualization, Methodology, Investigation, Software, Validation, Formal analysis, Writing - Original Draft. **Anne-Laure Ménard**: Investigation, Writing - review & Editing. **Lingyu Yue**: Software, Validation (mechanical tests), Writing - review & Editing. **Maryam Hajizadeh**: Validation (biomechanical tests), Writing - review & Editing. **Mickael Begon**: Conceptualization, Writing - review & Editing, Funding acquisition, Co-supervision. **Martin Lévesque**: Conceptualization, Writing - review & Editing, Resources, Funding acquisition, Supervision.

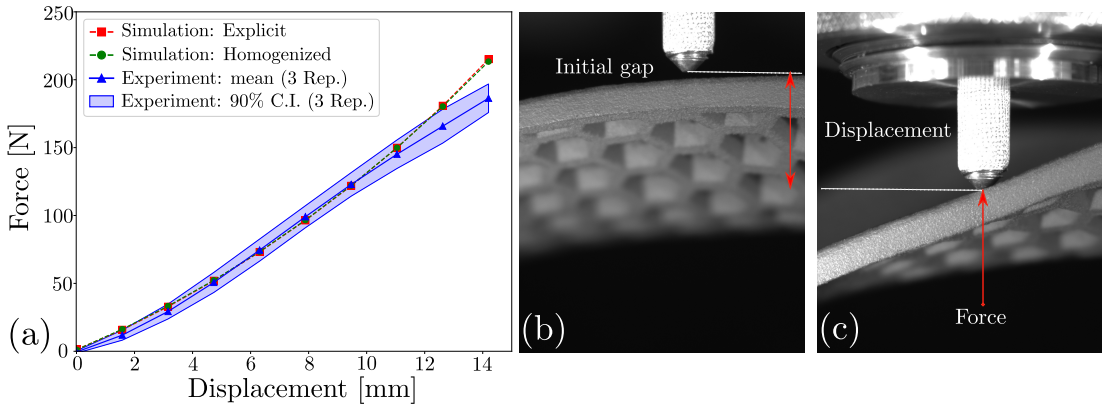

Figure 19: Validation of the simulations to predict the reaction force versus the vertical displacement of the punch; (a) the predicted and experimentally measured force-displacement curves, (b) the punch position before applying loading, (c) the punch position after applying loading. In the initial position of the punch in figure (b), there was a gap between the punch and the insole which was removed in plot (a). The measured force in figure (a) corresponds to the mean of three repetitions of the experiment. The predicted forces come from the explicit model as well as the homogenized model having relative differences of 9.77% and 9.27% respectively, against the experimentally measured force. The predicted forces are close together with a relative difference of less than 1.0%.

8 Acknowledgments

The authors greatly acknowledge Jacinte Bleau for enabling the manufacturing of the specimens, Ilyass Tabiai for his help in the DIC technique, Kambiz Chizari for his guidance in the tensile test and Véronica Rabanal-Duchesne for her help to prepare the CAD files. This research was also financially supported by NSERC R&D Coop with Médicus, Caboma and MEDTEQ [grant number RDCPJ 506194-16].

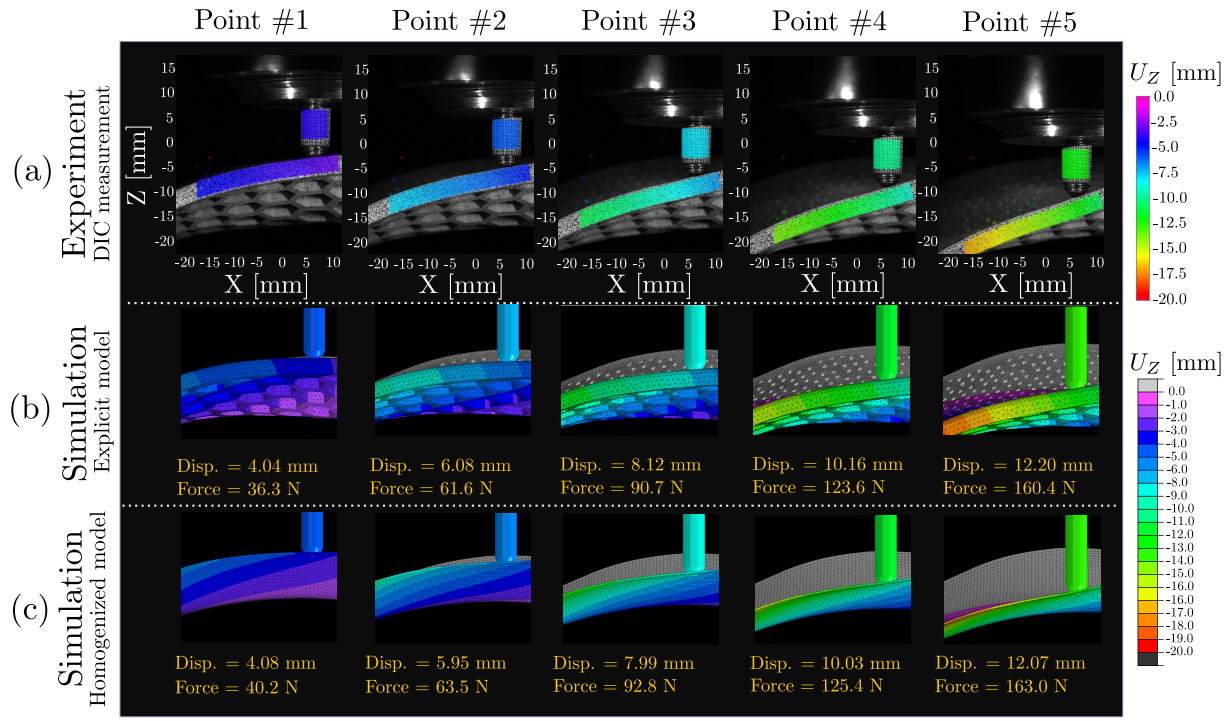

Figure 20: Validation of the predicted U_Z distribution of a honeycomb insole having a relative density of 40% and under the concentrated force of a punch during five time frames of the loading history including the applied displacements of $D = 4, 6, 8, 10$ and 12 mm over the punch; (a) the experimental measurement, (b) the predictions by the explicit model, (c) the predictions by the homogenized model. In Figure (c) the shell's thickness in the homogenized model is expanded by 10%.

A Numerical stability of discretization of height

The explicit model was employed to evaluate the performance of the homogenized model having different segmentations of variable h_2 including $\Delta_x = \Delta_y = 28, 24, 20, 16, 12, 8$ and 4 mm to predict U_Z when the honeycomb insole was under the foot pressure. Figure 23 shows the discretization and Figure 24 shows the norm-2 of the difference between the predicted U_Z normalized by the norm-2 of the explicit model's prediction (*i.e.* $\frac{||U_Z^{\mathrm{E}} - U_Z^{\mathrm{Hmg.}}||_2}{||U_Z^{E}||_2}$). The result confirms the numerical stability of such discretization scheme since the discrepancies of the homogenized model's predictions do not grow unbounded by decreasing the segments.

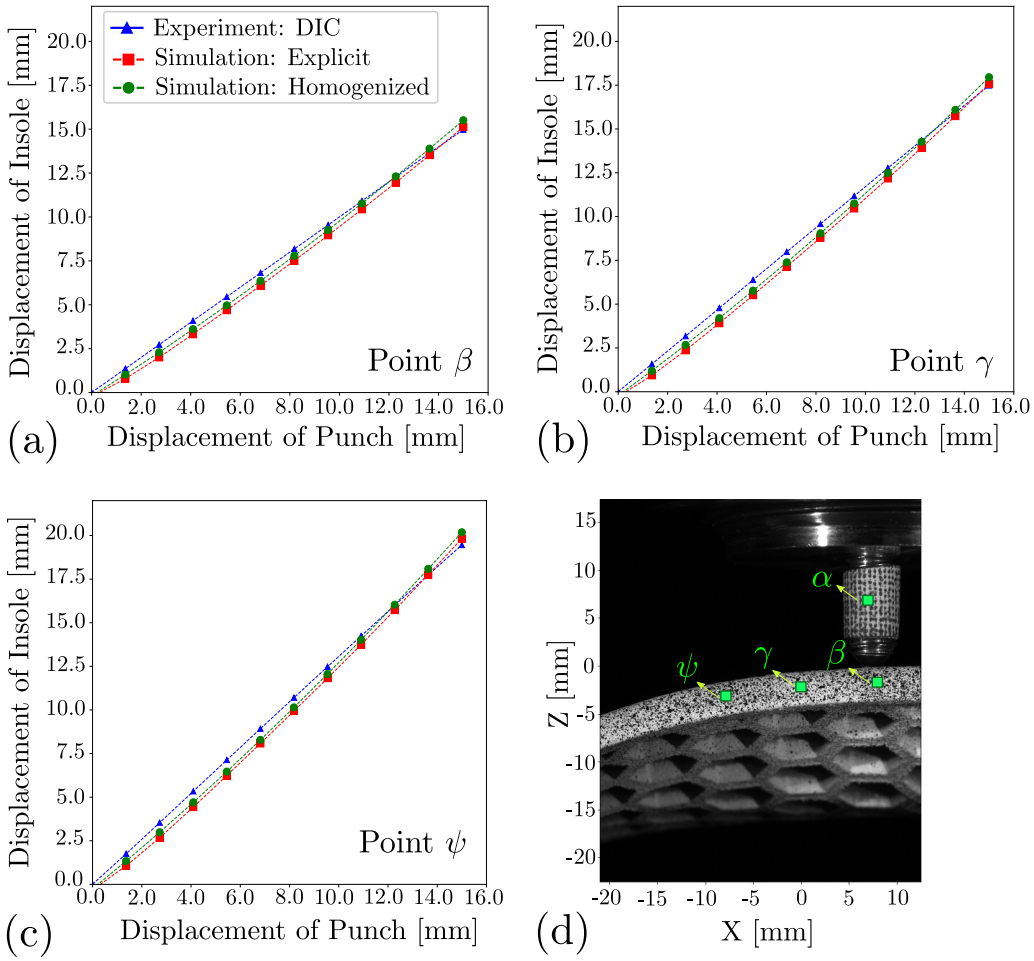

Figure 21: Validation of the explicit and the homogenized models to predict the vertical displacement U_Z over (a) point β, (b) point γ, (c) point ψ within (d) the area of interest in the Digital Image Correlation measurement. In this validation, the maximum discrepancy of the explicit model's prediction is 6.32% which is over point β, and, for the homogenized model, it is 4.33% over the point ψ.

References

[1] Desmyttere, G., Hajizadeh, M., Bleau, J., and Begon, M. *Clinical Biomechanics* **59**, 117–129 (2018).

[2] Schaper, N., Van Netten, J., Apelqvist, J., Lipsky, B., Bakker, K., and on the Diabetic Foot (IWGDF), I. W. G. *Diabetes/metabolism research and reviews* **32**, 7–15 (2016).

[3] Telfer, S. and Woodburn, J. *Journal of foot and ankle research* **3**(1), 19 (2010).

[4] Desmyttere, G., Hajizadeh, M., Bleau, J., Leteneur, S., and Begon, M. *Clinical Biomechanics* **86**, 105390 (2021).

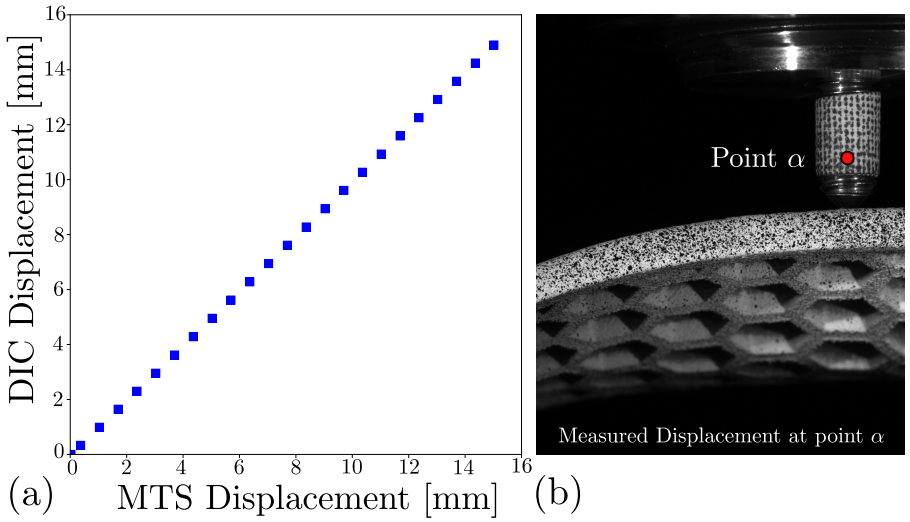

Figure 22: Verification of the measured displacement; (a) measured vertical displacement by DIC versus MTS machine's measurement, (b) the position of point α where the vertical displacement was extracted using DIC. The relative difference between two measurements is 1.02%. Both measurements are accepted to be used for the validation.

[5] Ma, Z., Lin, J., Xu, X., Ma, Z., Tang, L., Sun, C., Li, D., Liu, C., Zhong, Y., and Wang, L. *International Journal of Lightweight Materials and Manufacture* **2**(1), 57–63 (2019).

[6] Tang, L., Wang, L., Bao, W., Zhu, S., Li, D., Liu, C., et al. *Journal of the mechanical behavior of biomedical materials* **94**, 279–287 (2019).

[7] Sorohan, S., Constantinescu, D. M., Sandu, M., and Sandu, A. G. *Mechanics of Materials* **119**, 74–91 (2018).

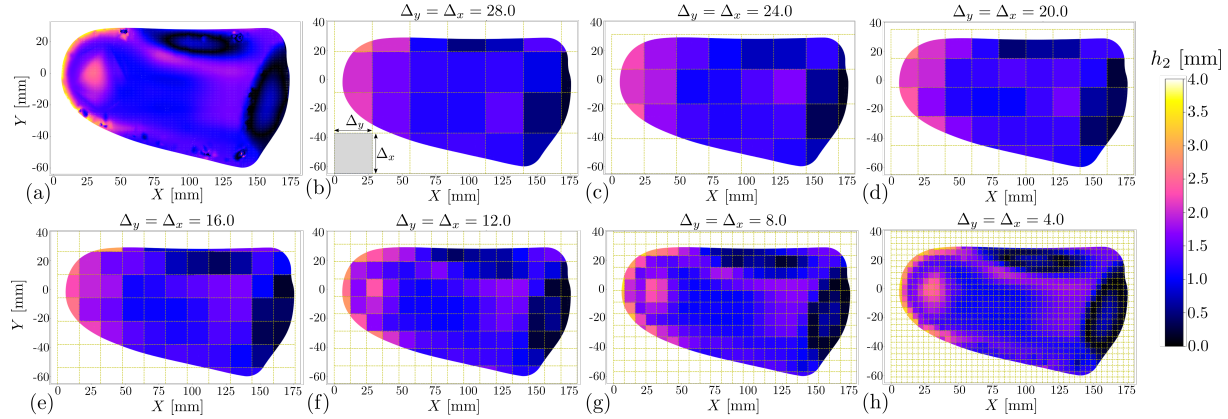

Figure 23: Modelling of variable height h_2; (a) the reference distribution is discretized by (b) 28 mm, (c) 24 mm, (d) 20 mm, (e) 16 mm, (f) 12 mm, (g) 8 mm and (h) 4 mm.

[8] Quevedo González, F. J. and Nuño, N. *Computer methods in biomechanics and biomedical engineering* **19**(8), 845–854 (2016).

[9] Coenen, E. W., Kouznetsova, V. G., and Geers, M. G. *International Journal for Numerical Methods in Engineering* **83**(8-9), 1180–1205 (2010).

[10] Moayedi, M., Arshi, A., Salehi, M., Akrami, M., and Naemi, R. *Computers in Biology and Medicine* **135**, 104598 (2021).

[11] Michaud, B. and Begon, M. *Journal of Open Source Software* **6**(57), 2562 (2021).

[12] Tawhai, M., Bischoff, J., Einstein, D., Erdemir, A., Guess, T., and Reinbolt, J. *IEEE Engineering in medicine and biology magazine* **28**(3), 41–49 (2009).

[13] Hassani, B. and Hinton, E. *Computers & Structures* **69**(6), 707–717 (1998).

[14] Qiu, C., Guan, Z., Jiang, S., and Li, Z. *Chinese Journal of Aeronautics* **30**(2), 766–779 (2017).

[15] Martínez-Ayuso, G., Friswell, M. I., Adhikari, S., Khodaparast, H. H., and Berger, H. *International Journal of Solids and Structures* **113**, 218–229 (2017).

[16] Andreassen, E. and Andreasen, C. S. *Computational Materials Science* **83**, 488–495 (2014).

[17] Kanit, T., Forest, S., Galliet, I., Mounoury, V., and Jeulin, D. *International Journal of solids and structures* **40**(13-14), 3647–3679 (2003).

[18] Gusev, A. A. *Journal of the Mechanics and Physics of Solids* **45**(9), 1449–1459 (1997).

[19] Barello, R. B. and Lévesque, M. *International Journal of Solids and Structures* **45**(3-4), 850–867 (2008).

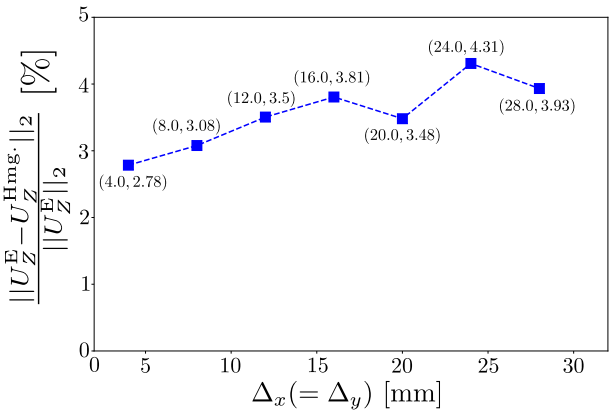

Figure 24: The discrepancy of the homogenized model to predict the displacement U_Z when compared to the predictions of the explicit model. The results show the numerical stability of the discretization of h_2.

[20] Barbero, E. J. *Finite element analysis of composite materials using ANSYS*. CRC press, (2013).

[21] Moussaddy, H., Therriault, D., and Lévesque, M. *International Journal of Solids and Structures* **50**(24), 3817–3828 (2013).

[22] Hajizadeh, M., Desmyttere, G., Ménard, A.-L., Bleau, J., and Begon, M. *Gait & Posture* **91**, 117–125 (2022).

[23] Han, K., Bae, K., Levine, N., Yang, J., and Lee, J.-S. *Medical science monitor: international medical journal of experimental and clinical research* **25**, 5920 (2019).

[24] Xu, R., Wang, Z., Ren, Z., Ma, T., Jia, Z., Fang, S., and Jin, H. *Medical science monitor: international medical journal of experimental and clinical research* **25**, 3510 (2019).

[25] Balsdon, M., Dombroski, C., Bushey, K., and Jenkyn, T. R. *Prosthetics and orthotics international* **43**(3), 331–338 (2019).

[26] Hajizadeh, M., Michaud, B., Desmyttere, G., Carmona, J.-P., and Begon, M. *PloS one* **15**(5), e0232677 (2020).

[27] Malek, S. and Gibson, L. *Mechanics of Materials* **91**, 226–240 (2015).

[28] Wang, A.-J. and McDowell, D. *Journal of engineering materials and technology* **126**(2), 137–156 (2004).

[29] Schmid, M., Amado, A., and Wegener, K. In *AIP Conference proceedings*, volume 1664, 160009. AIP Publishing LLC, (2015).

[30] Tekieli, M., De Santis, S., de Felice, G., Kwiecień, A., and Roscini, F. *Composite Structures* **160**, 670–688 (2017).

[31] Tabiai, I., Tkachev, G., Diehl, P., Frey, S., Ertl, T., Therriault, D., and Lévesque, M. *Engineering Fracture Mechanics* **216**, 106485 (2019).

[32] Cherni, Y., Desmyttere, G., Hajizadeh, M., Bleau, J., Mercier, C., and Begon, M. *Clinical Biomechanics* , 105553 (2021).

[33] Moeini, M., Begon, M., and Lévesque, M. *Mechanics of Materials* , 104210 (2022).

[34] Sharma, D. S. *International Journal of Mechanical Sciences* **65**(1), 115–124 (2012).

[35] Romanowicz, P. J., Szybiński, B., and Wygoda, M. *Materials* **13**(16), 3460 (2020).

[36] Van Hooreweder, B., Moens, D., Boonen, R., Kruth, J.-P., and Sas, P. *Polymer Testing* **32**(5), 972–981 (2013).

[37] Van Hooreweder, B. and Kruth, J.-P. *CIRP Annals* **63**(1), 241–244 (2014).